Chapter 21 – EXPERIMENTAL INVESTIGATIONS ON THE VFE-2 CONFIGURATION AT TU MUNICH, GERMANY

by

Andrej Furman[1] and Christian Breitsamter[2]

This report presents an overview of experimental investigations on a 65 deg swept delta wing as part of the International Vortex Flow Experiment 2 (VFE-2). Results obtained in low-speed wind tunnel facilities include oil flow and laser light sheet flow visualization, mean and unsteady surface pressure distributions as well as mean and turbulent velocity components of the flow field and close to the wing surface. Details of the delta wing vortex structure and breakdown phenomenon are discussed and analyzed. Special emphasis is on the occurrence of an inner vortex detected for the low Reynolds number and Mach number regime.

21.1 NOMENCLATURE

AR	aspect ratio
$\bar{c}_p$	mean pressure coefficient
$\hat{c}_p$	amplitude of pressure coefficient spectrum
c_{prms}	root mean square pressure coefficient
d_d	diameter of pressure probe
f	frequency
f_{dom}	dominant frequency
f_n	lens focal length number
k	reduced frequency, $f \cdot \bar{c} / U_\infty$
k_{dom}	dominant reduced frequency
l	length
p	static pressure
p_∞	free stream static pressure
q	dynamic pressure
s	wing semi span
S_{cp}	power spectrum of pressure coefficient fluctuations
S_{cp}^N	non-dimensional power spectrum of pressure coefficient fluctuations
S_p	power spectrum of pressure fluctuations
$S_{u_i'}$	power spectrum of velocity fluctuations

[1] Dipl.-Ing.

[2] PD Dr.-Ing. habil.

$S_{u_i'}^N$	non-dimensional power spectrum of velocity fluctuations
t	time
t_M	measurement time
Δt	pulse delay
T	temperature
u, v, w	axial, lateral and vertical velocities
$\overline{u}_i$	mean velocity components
u_i'	velocity fluctuations
$u_{i_{rms}}$	root mean square velocity components
$\overline{u_i' u_j'}$	turbulent shear stresses
U_∞	free stream velocity
X_p	Fourier transformed quantity of pressure fluctuation
$X_{u_i'}$	Fourier transformed quantity of velocity fluctuations
φ	leading-edge sweep
ρ	density

21.2 INTRODUCTION

Aerodynamic investigations of flow phenomena over generic and complex delta wing configurations have been performed for many years [[21-1]-[21-7], [21-15]-[21-19]]. The typical and well known delta wing flow physics is as follows: The flow separates already at low angles of attack at the highly swept leading-edges. The separated shear layer rolls up to form a large-scale vortex located over each half of the wing. Thus, two strong vortices influence the flow field of the wing upper side. Vortex formation along the leading-edge starts from the rear part to the apex. This primary vortex is fully developed when vorticity feeding exists over the entire leading-edge. The vortex cross flow area reveals a rotational core with an embedded subcore, the latter dominated mainly by viscous effects. The subcore is characterized by high axial velocities, low static pressures and enhanced velocity fluctuations due to the steep gradient in the cross flow components. The mean velocities on the wing upper surface are strongly increased by the leading-edge vortices resulting in high suction levels. The corresponding suction peaks in the spanwise pressure distribution indicate the track of the vortex axis on the wing surface. Therefore, leading-edge vortices in a fully developed, stable stage create additional lift and an increase in maximum angle of attack improving significantly maneuver capabilities of high-agility aircraft.

Sharp leading-edge configurations are often used in delta wing research work because primary separation is fixed and leading-edge vortex evolution is less sensitive to Reynolds number effects. Vortex aerodynamics becomes much more complicated for rounded or blunt leading-edge configurations as the position of primary separation varies to a certain extent depending on pressure gradient and boundary layer development. Thus, leading-edge radius, angle of attack and Reynolds number are the main parameters influencing the onset of vortex evolution as well as position and strength of the primary vortex whereas the angle of attack is the main parameter for the sharp leading-edge case only. There is a strong increase in the surface pressure when moving in spanwise direction from the station of the primary vortex suction peak to the leading-edge. This severe lateral pressure gradient provokes boundary layer separation in that region. The separated boundary layer rolls up by self induction and creates a small vortex, named secondary vortex, the rotation of which is opposite to that of the

leading-edge (primary) vortex. The formation of the secondary vortex depends strongly on the presence of a laminar or turbulent boundary layer [21-21]. Size and position of the secondary vortex affects the primary vortex location and, thus, the associated suction level.

Further, leading-edge vortices are subject to breakdown at high angles of attack. Vortex breakdown is caused by the stagnation of the low-energy axial core flow due to the increase of the adverse pressure gradient along the vortex axis with increasing angle of attack. This rise in the vortex core static pressure at the wing rear part is caused on the one hand by the diverging vortex subcore and on the other hand by the recompression in the trailing-edge area. Vortex breakdown is indicated by the rapid expansion of the vortex core accompanied by high velocity fluctuations. Downstream of breakdown, the fluctuation maxima are located in a limited radial range around the burst vortex core. In addition, the breakdown flow exhibits specific instability mechanisms leading to narrow-band unsteady aerodynamic forces [[21-1], [21-2], [21-15]]. The numerical simulation and analysis of the breakdown flow is still a challenging problem which needs the correct representation of the turbulent flow field and instability characteristics.

Euler methods were intensively developed in the 1980's, also aimed to calculate leading-edge vortex flows. Therefore, an experimental data base was needed for code validation and assessment established in frame of the International Vortex Flow Experiment 1 (VFE-1; 1984 – 1986). The tests included force and pressure measurements as well as flow field studies on a 65 deg swept cropped delta wing carried out in several wind tunnel facilities [21-10]. But Euler code results do not represent secondary vortices limiting the accuracy even for fixed primary vortices at sharp leading edges. The vortex induced surface pressure distribution is sensitive to viscous effects on the wing as well as in the rolled-up shear layers. Great efforts have been made in the last decade to develop and use high fidelity computational fluid dynamics methods. Unsteady Reynolds Averaged Navier-Stokes (URANS) Methods are available including a variety of turbulence models of algebraic type up to Reynolds stress transport equations. Further, methods of Detached Eddy Simulations (DES) are used as a combination of a Large Eddy Simulation (LES) to model separated flow dominated by large-scale structures in the outer domain and a turbulence model to calculate flow quantities in the wall-bounded domain. With such high fidelity methods available [[21-8], [21-9], [21-24]-[21-27]], there is again a strong need for an extended experimental data base. Consequently, a second International Vortex Flow Experiment (VFE-2) has been initiated. The VFE-2 activities are coordinated by the task group 113 of the Applied Vehicle Technology panel (AVT) of the NATO Research Technology Organization (RTO) named "Understanding and modeling of vortical flows to improve the technology readiness level for military aircraft" [21-20]. Latest test techniques are applied to gather high quality data. The research activities have been started in 2004 by partners of industry, research establishments and universities from Europe and the United States. The work is still on-going.

The Institute of Aerodynamics (AER) of the Technische Universität München (TUM) is part of the RTO AVT-113 task group focusing particularly on flow field turbulence and boundary layer quantities [11-14]. Both sharp and rounded leading edges are investigated. The tests are conducted on a new delta wing model which has been manufactured based on a NASA wing geometry served as reference configuration for VFE-2 [21-7]. The TUM-AER investigations have been performed in low-speed wind tunnel facilities using laser light sheet and oil flow visualization, steady and unsteady surface pressure measurements, stereo particle image velocimetry and hot-wire anemometry. The results are presented as distributions of mean, turbulent and spectral quantities, which give detailed information of the flow characteristics over the delta wing.

21.3 EXPERIMENTAL SET-UP

21.3.1 Facility

The measurements have been carried out in the low-speed wind tunnels A and B of the Institute of Aerodynamics at the Technische Universität München [21-11]. The wind tunnels are of closed-return type with an open test section. The free stream turbulence intensity is less than 0.4%. The uncertainty in the temporal and spatial mean velocity distribution is less than 0.6%. The uncertainty in free stream direction is below 0.2 deg and static pressure variations along the tunnel axis are below 0.4%.

21.3.2 Model

The present delta wing model [21-11] was designed to study leading-edge vortex flow features comparing sharp and rounded leading edges. The present model has a root chord length of c_r = 0.980 m, a wing span of b = 0.914 m, a leading edge sweep of φ = 65°, a wing area of S = 0.448 m^2 and an aspect ratio of AR = 1.86. The wing was designed using a CAD tool and then given to the manufacturer as digital three-dimensional model. The delta wing consists of an upper and a lower base plate, the trailing edge with a depth of x_{TE}/c_r = 10% and the pressure orifices being part of these plates. On the inside of these plates cut-outs are milled to house the tubes and wires from the pressure orifices and unsteady pressure transducers. The thickness is t = 0.033m, which is constant over the base plate. A sharp and a rounded leading edge ($r_{LE,rounded}$, $/\bar{c}$ = 0.0015) are available, r_{LE} being the leading edge radius and $\bar{c}$ the mean aerodynamic chord. The leading edges are fitted on the left and right hand side of the lower base plate and have a depth of x_{LE}/c_r = 15%. On each of the leading edge elements, five pockets for the pressure sensors have been milled, which are closed with separate lids. On the mounted wing a model sting is installed, which is attached to the three-axis model support via a model adapter. All parts are manufactured from aluminium "Certal" and, therefore, enabling measurements in cryogenic wind tunnels also. There are 177 pressure orifices with a diameter of d = 0.3 mm situated on the entire wing, 44 are equipped with unsteady pressure sensors. The pressure orifices are positioned in five chordwise positions (x/c_r = 0.2, 0.4, 0.6, 0.8 and 0.95).

21.3.3 Test Cases

The investigations have been carried out for three angles of attack, namely at:

- α = 13° for partly developed;
- α = 18° for fully developed; and
- α = 23° for burst leading-edge vortices.

The test Mach numbers (Table 21-1) for all cases are M = 0.07 and M = 0.14 and the corresponding Reynolds numbers based on the mean aerodynamic chord are R_{mac} = 1 x 10^6 and R_{mac} = 2 x 10^6, respectively. Except for the laser light sheet measurements, which have been obtained at Mach number M = 0.035 and a Reynolds number of R_{mac} = 0.5 x 10^6.

Table 21-1: Test Cases of the TU München

Measurements	Sections x/c_r	Angle of Attack	Reynolds Number	Mach Number
PSI	0.2 / 0.4 / 0.6 / 0.8 / 0.95	0° – 30°	1×10^6 / 2×10^6	0.07 / 0.14
Unsteady Pressure	0.4 / 0.6 / 0.8 / 0.95	0° – 30°	1×10^6 / 2×10^6	0.07 / 0.14
Laser Light Sheet Visualisation	0.2 / 0.4 / 0.6 / 0.8 / 0.95 / 1.1	0° – 30°	0.5×10^6	0.035
	upper surface $z/c_r = 0.01$			
	upper surface $z/c_r = 0.041$			
Oil Visualisation	surface streamlines	13° / 18° / 23°	0.5×10^6 / 1×10^6 / 2×10^6	0.035 / 0.07 / 0.14
Stereo PIV	0.2 / 0.4 / 0.6 / 0.8 / 0.95	13° / 18° / 23°	1×10^6 / 2×10^6	0.07 / 0.14
Hot-Wire Anemometry	0.4 / 0.6 / 0.8	13° / 18° / 23°	1×10^6	0.07

21.3.4 Measurement Techniques

During the project several measurement techniques have been used:

Laser light sheet visualization [21-12] is used in order to survey the flow field in a plane, which is illuminated by a laser beam expanded by a cylindrical lens. The smoke particles in this plane are then recorded with a digital photo camera. The particle size is approximately 2 µm, in order to guarantee sufficient light reflection. For this investigation an air cooled class 3B Argon-Ion-laser has been used. This laser has a maximum power of 100 mW and the wave length of the light is between 457 ÷ 514 nm.

Oil flow visualization [21-12] illustrates the surface stream lines on the suction side of the wing. A black foil was stuck on the model surface to achieve good visual contrast between oil flow pigments and background color. A mixture of yellow paint pigments, petrol and paraffin was applied on the upper surface and exposed to the free stream flow briefly. The developed flow picture was then photographed.

Surface pressure measurements [[21-4], [21-11], [21-12]]. The **steady** pressures are measured on the upper and lower surface of the wing at five chord stations with 133 measuring tabs in total. The sampling rate of the measured values is f = 100 Hz with an averaging time of t = 10 s. The **unsteady** pressure measurements were accomplished in four chord stations on the suction side of the wing with 12 unsteady pressure sensors per chord station. A sampling rate of f = 2000 Hz and a sample time of t = 40 s is used. The frequency of the measurement system low-pass filter was set to 256 Hz.

Stereo Particle Image Velocimetry (Stereo-PIV) [[21-13], [21-14]] is performed with two cameras left and right of a laser light sheet. A pair of 135 mm, $f_n = 2.8$ objective lenses constitute the recording optics and are connected to the charge coupled device (CCD) camera with 1600 x 1186 pixel resolution. The light sheet was generated by a frequency doubled, double oscillator Nd-YAG laser with a maximum energy level of 200 mJ and a frequency of 10 Hz per pulse. The light sheet thickness was set at approximately 10 mm and the pulse delay was set to $\Delta t = 21$ µs.

Hot-Wire Anemometry (HWA) [[21-2], [21-13], [21-14]] is based on a dual-sensor probe of cross-wire type for measuring the fluctuating velocities. The probes were operated by a multi-channel constant-temperature anemometer system. By means of its signal conditioner modules, bridge output voltages were low-pass filtered at 1000 Hz before digitization and amplified for optimal signal level. The sampling time for each channel is 6.4 s, with the sampling rate set to 3000 Hz (Nyquist frequency of 1500 Hz), so that each sample block contains 19200 values. The use of cross-wires generally assumes some knowledge of the flow field, such as a known flow direction to which the probe must be aligned. To determine the three velocity components, the probe has to be rotated around its axis by 90 deg to adjust the wire plane once horizontal and once vertical against the main flow direction. Thus, two triggered traverse sweeps are necessary to obtain the streamwise u, lateral v and vertical w velocity components, respectively. Each digitized and temperature corrected voltage pair of the corresponding probe positions was converted to evaluate the time-dependent velocity vector. The numerical method used is based on look-up tables derived from the full velocity and flow angle calibration of the probe [21-2].

21.4 ANALYSIS OF RESULTS

The discussion and analysis of the measurement results address flow topology, mean and fluctuating surface pressures, mean and fluctuating flow field and boundary layer velocities and spectral quantities.

21.4.1 Flow Topology

21.4.1.1 Flow Field

Laser light sheet visualization can be used to determine the flow behaviour above and behind the wing as well as the size and position of the vortices [[21-2], [21-12], [21-22]]. The pictures taken from behind the wing for the stations x/c_r = 0.2, 0.4, 0.6, 0.8, 0.95, and 1.1 are shown on the right hand side of Figure 21-1. They illustrate cross sections of the vortex. Pictures from above, i.e. parallel to the wing upper surface, at z/c_r = 0.01 and 0.05 are shown on the left hand side of Figure 21-1. Based on such images, the position of the leading-edge vortex center (trajectories of vortex axis) and the breakdown location at high angles of attack can be determined, Figure 21-8.

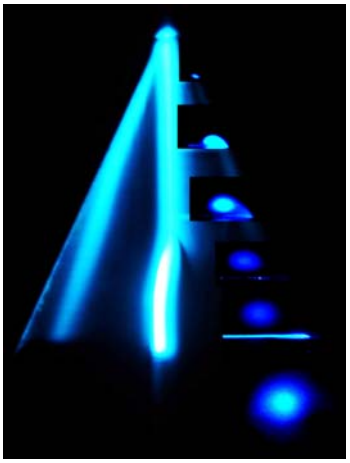

(a) α = 13°

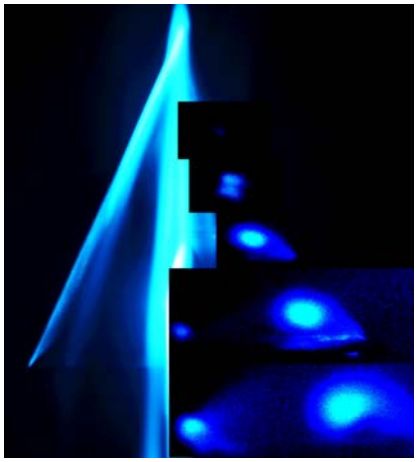

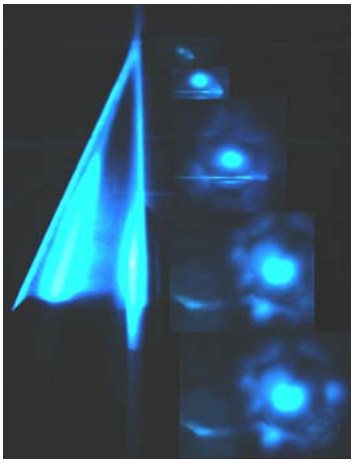

(b) α = 18°

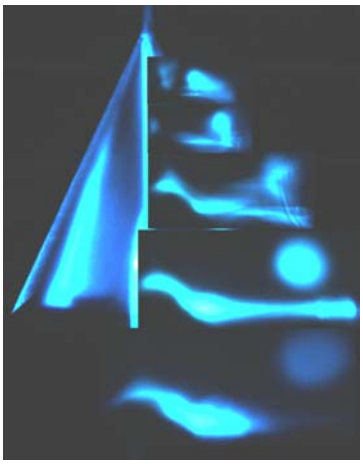

(c) α = 23°

Figure 21-1: Laser Light Sheets of Vortex Structure above and behind the Wing at R_{mac} = 5 x 10^5 and M = 0.035 for Sharp (left) and Rounded (right) Leading Edges.

Regarding Figure 21-1 (a), the partly developed leading-edge vortex at $\alpha = 13°$ is depicted where the primary separation at the sharp leading-edge has not yet reached the apex. Also, the area of the secondary vortex can be detected underneath the primary vortex close to the leading-edge. The comparison between sharp and rounded leading-edge shows a delayed separation for the rounded leading-edge, which is also indicated by a smaller vortex core and a stronger trailing-edge effect. Figure 21-1 (b) illustrates the fully developed vortex for $\alpha = 18°$ where some coherent vortical structures can be observed in the primary vortex feeding shear layer for the case of sharp leading-edge (Figure 21-1 (b) left). Vortex breakdown takes place in the rearward portion of the wing at $\alpha = 23°$ highlighted by the expanded core area for both sharp and rounded leading-edge.

21.4.1.2 Surface Flow

Concentrating again on the flow behaviour for the rounded leading-edge case at $\alpha = 13°$, the corresponding surface streamlines are shown by oil flow visualization, Figure 21-2. A schematic representation depicts the flow topology derived from the laser light sheet and oil flow pictures, Figure 21-4. This schematic highlights the separation and attachment lines of the primary and secondary vortex as indicated by the surface streamlines. The leading-edge (primary) vortex starts from a turbulent separation at the wing rear part, with the turbulent shear layers of the wing upper and lower side rolling up along the leading-edge. The roll-up process does not reach the apex at this angle of attack but progresses up to the wing front part. There, a laminar boundary layer is present. Transition is indicated by an outboard shift of the separation line of the secondary vortex. Further, a laminar separation exists near the apex close to the symmetry plane. This three-dimensional separation bubble is caused by the pressure increase when the flow has turned around the leading-edge contour of the relatively thick wing. Downstream, the inboard separated flow forms a small inner vortex favoured by the positive lateral pressure gradient. The inboard vortex rotates in the same direction as the leading-edge (primary) vortex. Separation and attachment line of the inboard vortex are positioned closely together and can be clearly seen in the oil flow picture. The inboard vortex extends over the entire chord length to the wing rear edge. Further tests have shown that the trajectory and strength of the inboard vortex depends strongly on angle of attack (strength of primary vortex and adverse lateral pressure gradient) and Reynolds number (area of laminar flow). Therefore, this phenomenon is only visible at certain Reynolds numbers in the medium angle of attack range, Figure 21-2 and Figure 21-3.

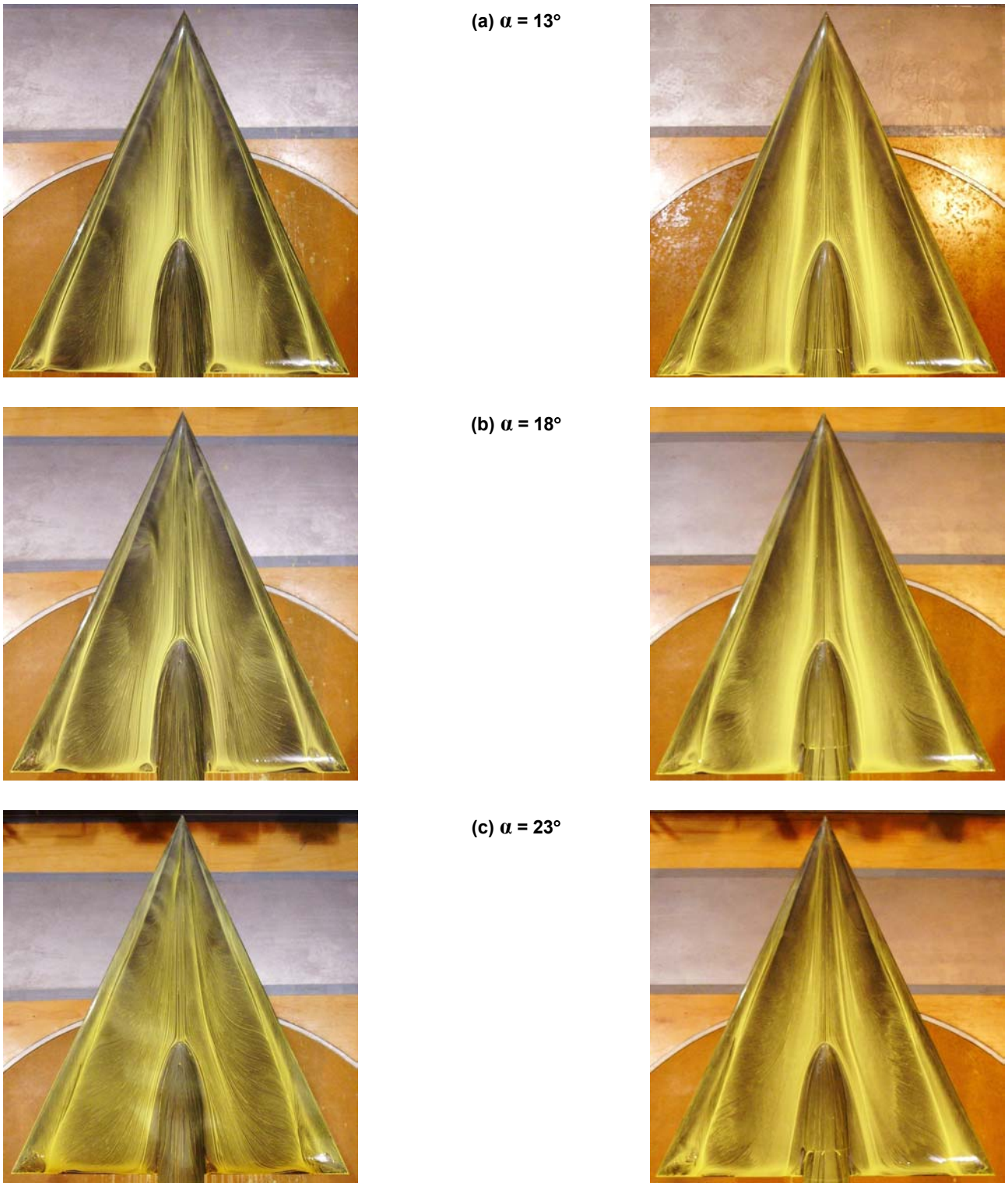

Figure 21-2: Surface Oil Flow Visualization at R_{mac} = 1 x 10^6 and M = 0.07 for Sharp (left) and Rounded (right) Leading Edges.

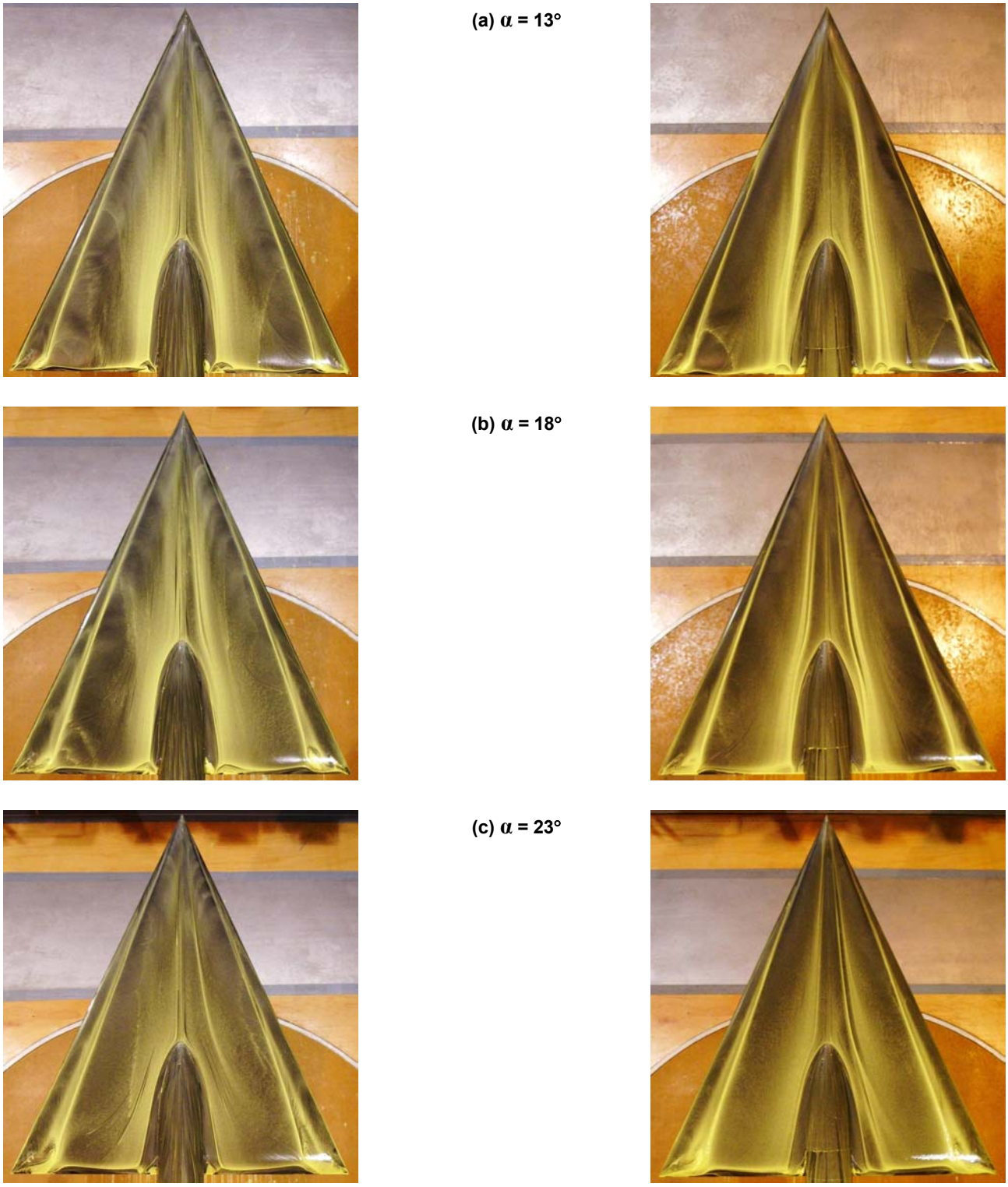

Figure 21-3: Surface Oil Flow Visualization at $R_{mac} = 2 \times 10^6$ and M = 0.14 for Sharp (left) and Rounded (right) Leading Edges.

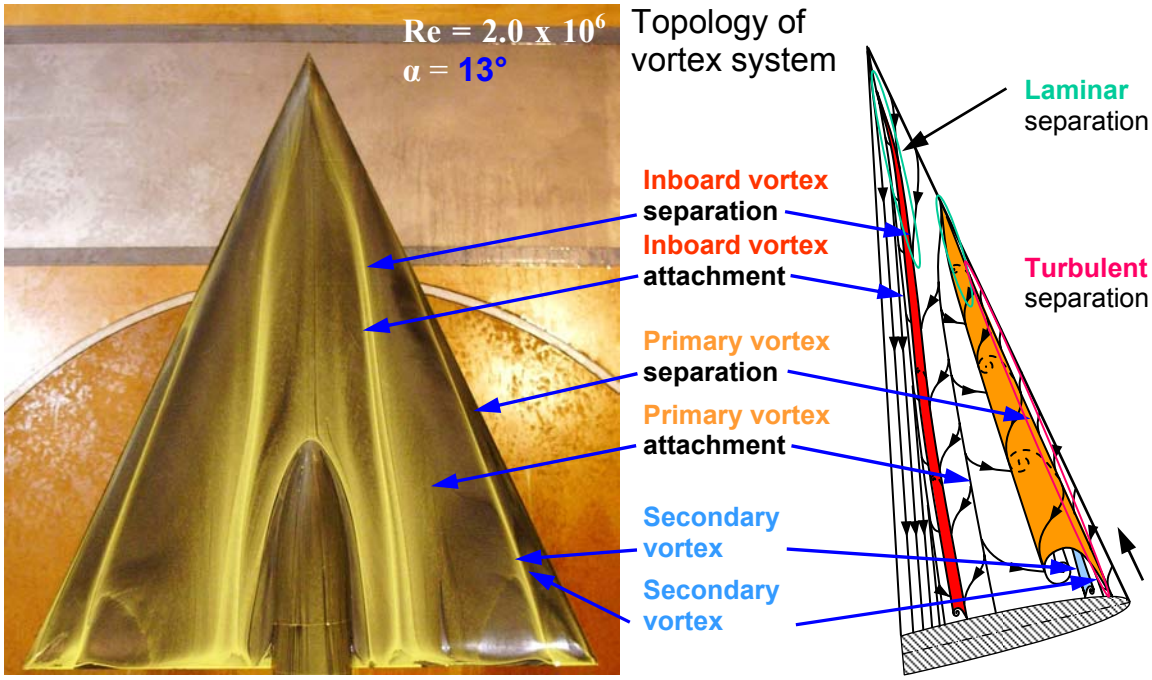

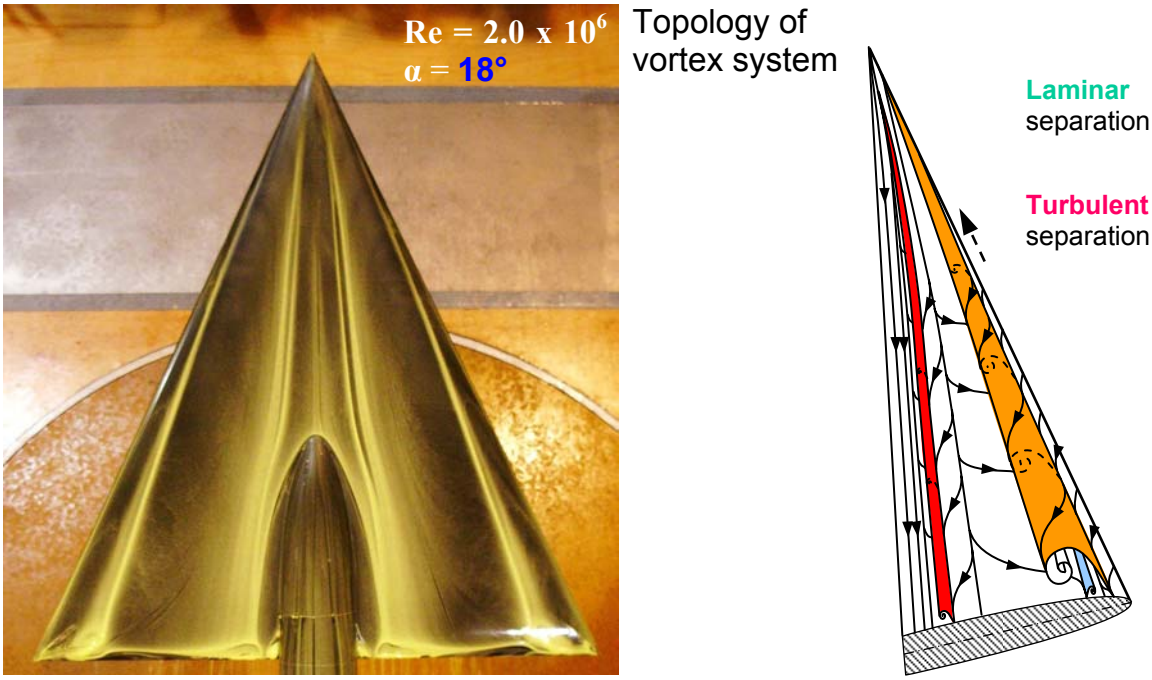

Figure 21-4: Flow Topology Based on Laser Light Sheet and Oil Flow Visualization for α = 13° and 18° at R_{mac} = 2 x 10^6.

21.4.2 Mean Flow Field

21.4.2.1 Pressure Distribution

For the time-averaged pressure coefficients the surface pressures p(P,t) at the position P are converted in non dimensional values. The pressure coefficient is defined by

$$c_p(P,t) = \frac{p(P,t) - p_\infty}{q_\infty} \tag{1}$$

where p(P,t) is the static pressure, p_∞ the static free stream pressure and q_∞ the dynamic pressure. For each position P on the upper wing surface the time series of the non dimensional pressure coefficient $c_p(P,t)$ are then available at every test condition.

The average of the pressure coefficient $\overline{c}_p(P,t)$ is defined as

$$\overline{c}_p(P) = \frac{1}{t_M}\int_0^{t_M} c_p(P,t)dt \tag{2}$$

where t_M is the time of measurement or the length of the time series.

Three steady measurement results are shown for α = 13°, α = 18° and α = 23° in Figure 21-5 and Figure 21-6. Each figure shows the development of the steady pressure distribution in several chordwise stations for the cases of sharp and rounded leading edge. Leading-edge separation occurring on a blunt or rounded leading-edge contour is a more complex phenomenon as the primary separation is no longer fixed to a geometric discontinuity as given by a sharp edge. Therefore, the onset of leading edge separation is determined by flow conditions and the particular wing geometry. For low to moderate angels of attack fully attached flow may be present. Leading-edge separation will first occur near the wing tip progressing then in direction to the apex with further increase in angle of attack. Consequently, the wing will exhibit partially developed leading-edge separation with attached flow on the upstream portion of the wing and leading-edge vortex formation on the downstream portion. The separation line of the primary vortex is free to move inboard or outboard depending on Reynolds number and Mach number conditions. This complexity in the flow physics can have considerable impact on the aerodynamic properties and maneuver performance of slender wing geometries. The correlation of separation onset for the present test conditions is summarized in Figure 21-10.

(a) α = 13°

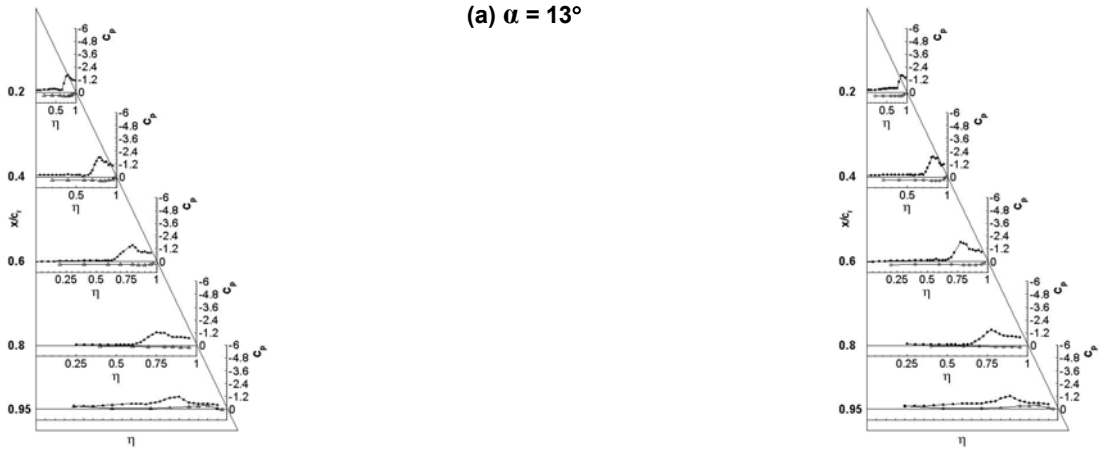

(b) α = 18°

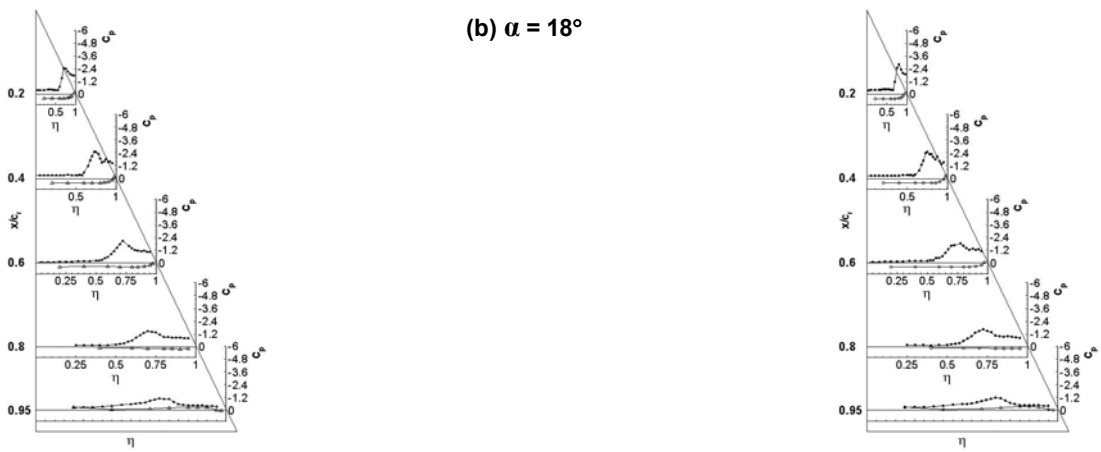

(c) α = 23°

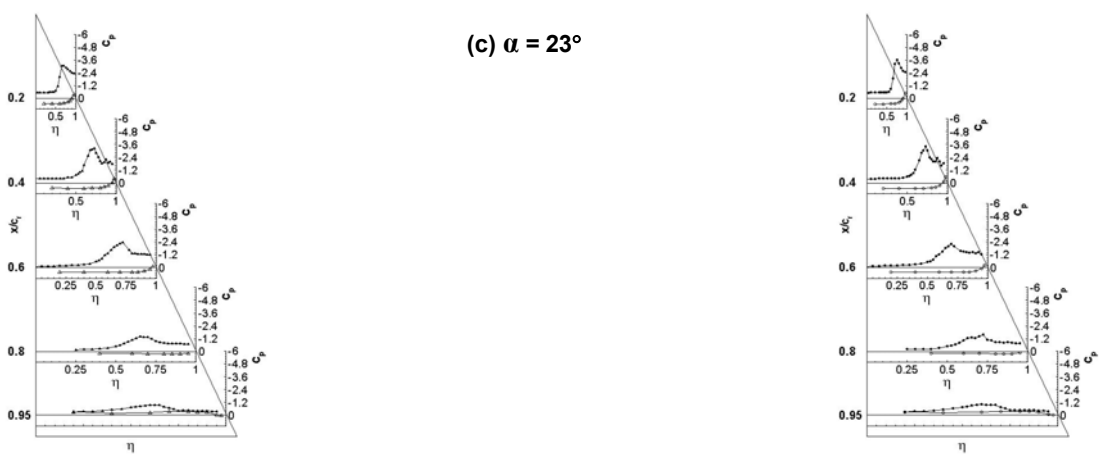

Figure 21-5: Steady Pressure Distribution at R_{mac} = 1 x 10^6 and M = 0.07 for Sharp (left) and Rounded (right) Leading Edges.

(a) α = 13°

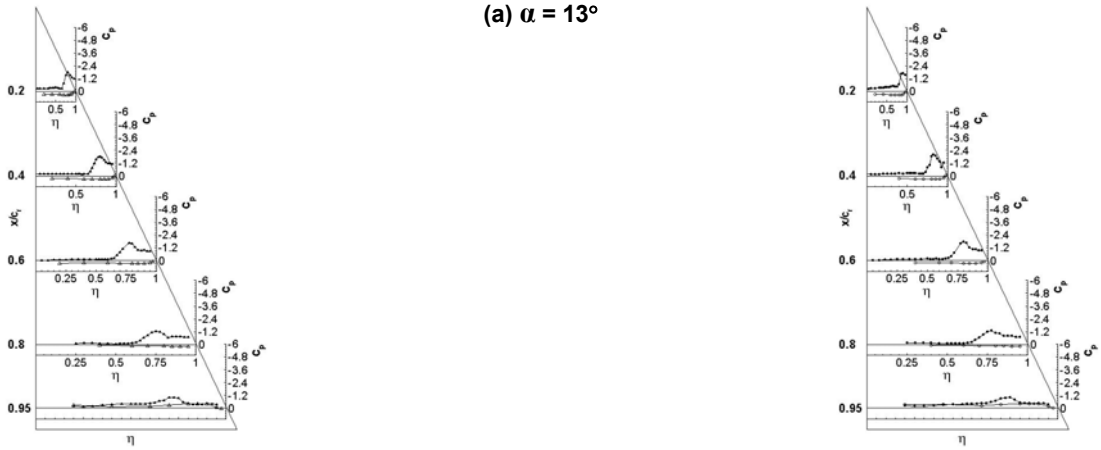

(b) α = 18°

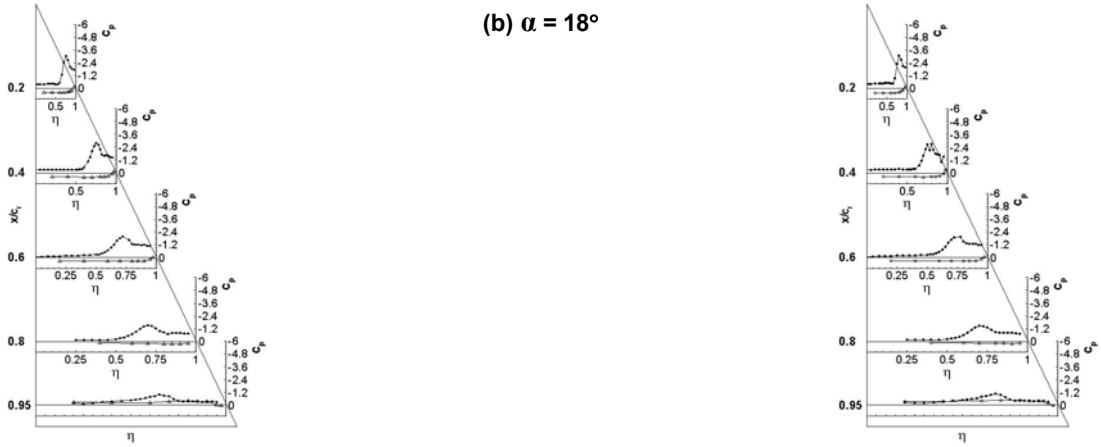

(c) α = 23°

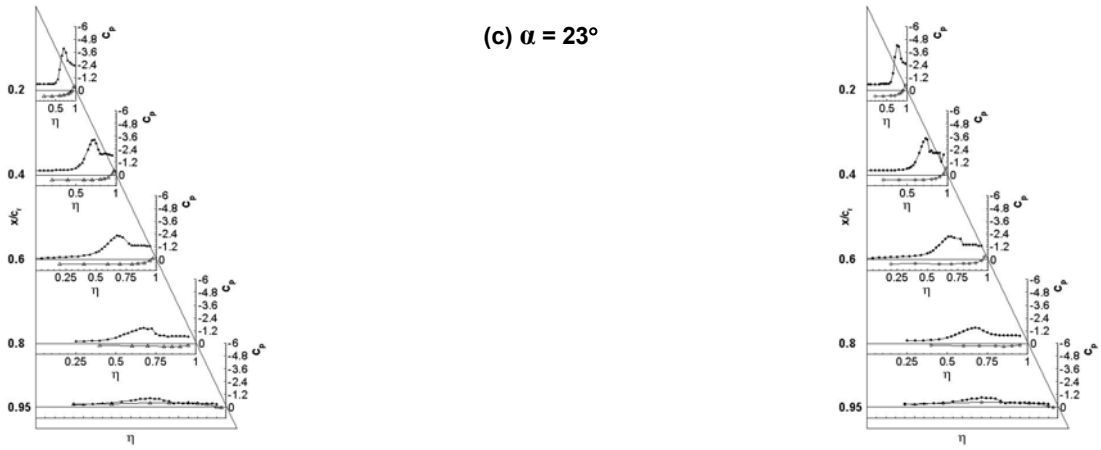

Figure 21-6: Steady Pressure Distribution at R_{mac} = 2 x 10^6 and M = 0.14 for Sharp (left) and Rounded (right) Leading Edges.

At α = 13° significant suction peaks are visible, marking the axis of the primary vortex, Figure 21-5 (a), Figure 21-6 (a). The suction peaks reduce with increasing chord station, except for the second station (x/c_r = 0.4), where the peak is slightly increased. This is due to the vortex not being fully developed at this angle of attack. The constant suction level over the inner wing area marks the region of reattachment. The secondary vortex is visible in all chord stations in form of a locally higher suction level outboard of the primary vortex, except for x/c_r = 0.2 for the rounded leading edge, where the secondary vortex is just forming. The suction peaks for the primary as well as for the secondary vortex also move inboard in the rear portion of the wing.

With increasing angle of attack, the suction peaks increase in all chord stations, Figure 21-5 (b), Figure 21-6 (b). The vortex diameter also increases, being evident in the suction peak broadening. The vortex axis moves inboard with increasing angle of attack and the reattachment lines are moved towards the wing center line.

Further increasing the angle of attack to α = 23°, the suction peaks also increase in the chord stations x/c_r = 0.2, 0.4 and 0.6, Figure 21-5 (c), Figure 21-6 (c). Chord stations further downstream show decreased suction peaks. At α = 18° the suction peaks at x/c_r = 0.8 are $C_{p,sharp,18°}$ = -1.51 and $C_{p,rounded,18°}$ = -1.44. Increasing the angle of attack to α = 23° reduces the suction peak for the sharp leading-edge case and stay on the same level for rounded leading-edge $c_{p,sharp,23°} \approx c_{p,rounded,23°}$ = -1.45. This is due to the vortex breakdown in this area [21-2]. Again, the primary vortex axes have been marked in Figure 21-10, also showing the position of vortex breakdown, which is slightly further upstream for the sharp leading edge. The position of primary vortex breakdown for the rounded leading edge was determined at $x/c_r \approx 0.8$ and for the sharp leading edge at $x/c_r \approx 0.75$.

The difference in the pressure distribution between the rounded and the sharp leading edge is most evident at x/c_r = 0.2 for all angles of attack illustrated here. This difference decreases with increasing chord station, Figure 21-7, disappearing completely at the aft station. The primary vortex for the rounded leading edge is located slightly further outboard than for the sharp leading edge. For an angle of attack of α = 23° the suction peak at x/c_r = 0.2 for the rounded leading edge is significantly higher than for the sharp leading edge. Increasing the angle of attack causes the pressure on the upper surface in the inboard area and also the pressure on the entire lower surface of the wing to slightly decrease. On the lower surface no significant difference between the sharp and the rounded leading edge is evident.

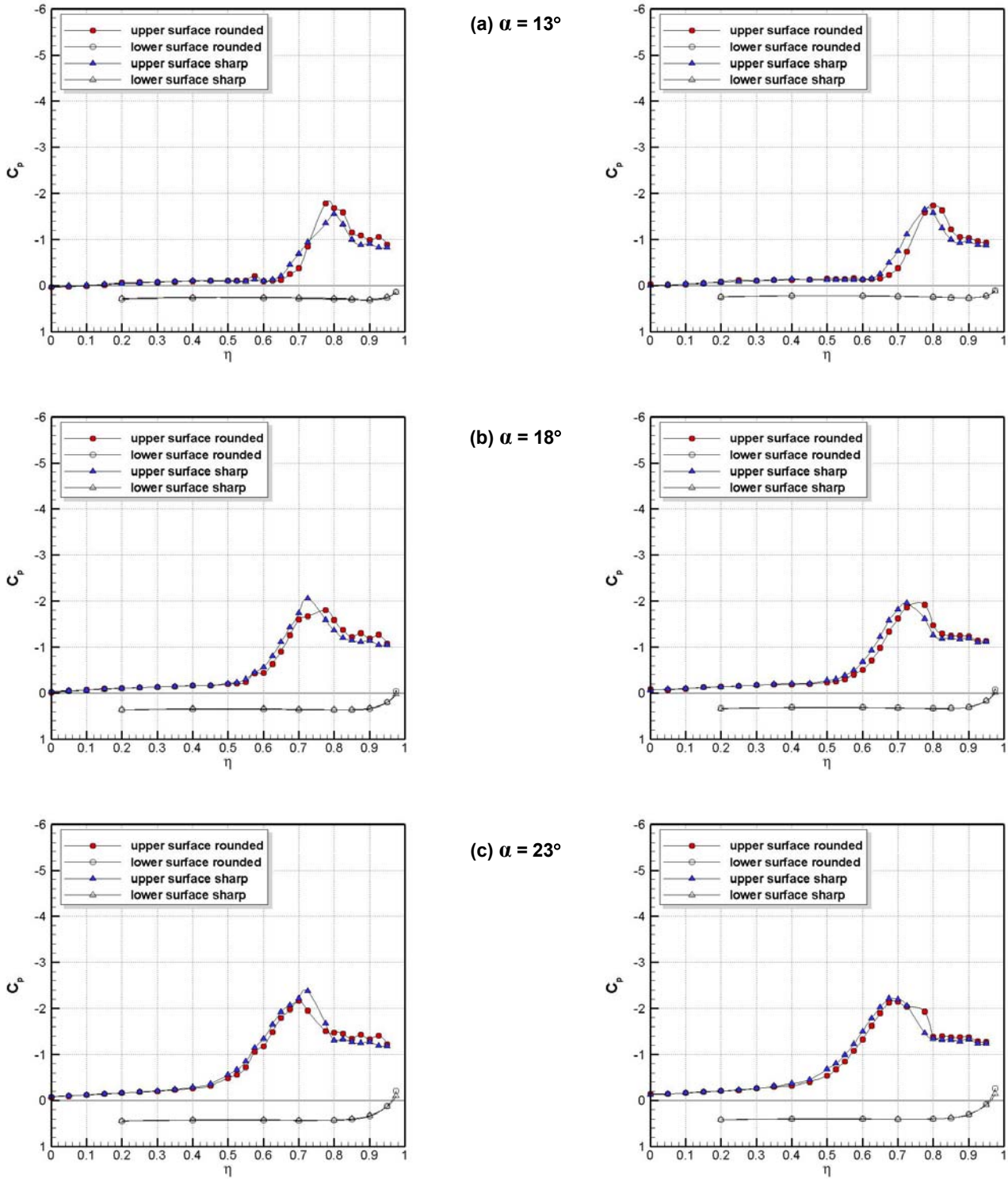

Figure 21-7: Comparison of Steady Pressure Distribution between Sharp and Rounded Leading Edge at R_{mac} = 1 x 10^6 (left) and R_{mac} = 2 x 10^6 (right) in Section x/c_r = 0.6.

The quality of TUM-AER measurements have been judged by comparison with steady pressure measurements obtained by NASA for the delta wing reference configuration [[21-7], [21-23]]. Figure 21-8 contains the NASA results for $R_{mac} = 2 \times 10^6$, M = 0.2 and the results obtained by TUM–AER for $R_{mac} = 2 \times 10^6$, M = 0.14. The comparison shows a very good agreement between the steady pressure distributions, which clearly illustrates the comparability in terms of free stream, wind tunnel and model conditions.

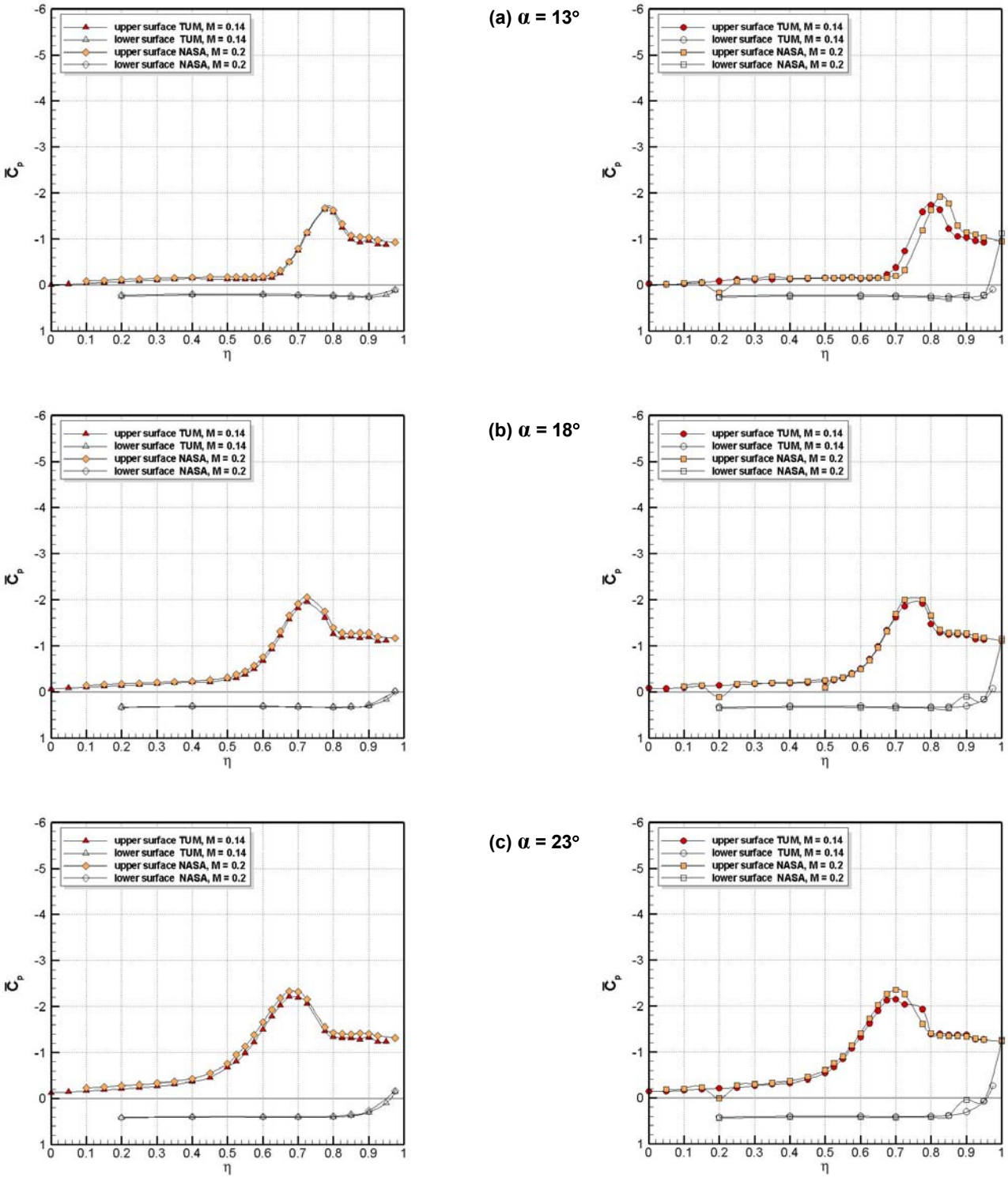

Figure 21-8: Comparison of Steady Pressure Distribution between NASA and TUM Measurements for Sharp (left) and Rounded (right) Leading Edge at $R_{mac} = 2 \times 10^6$ in Section $x/c_r = 0.6$.

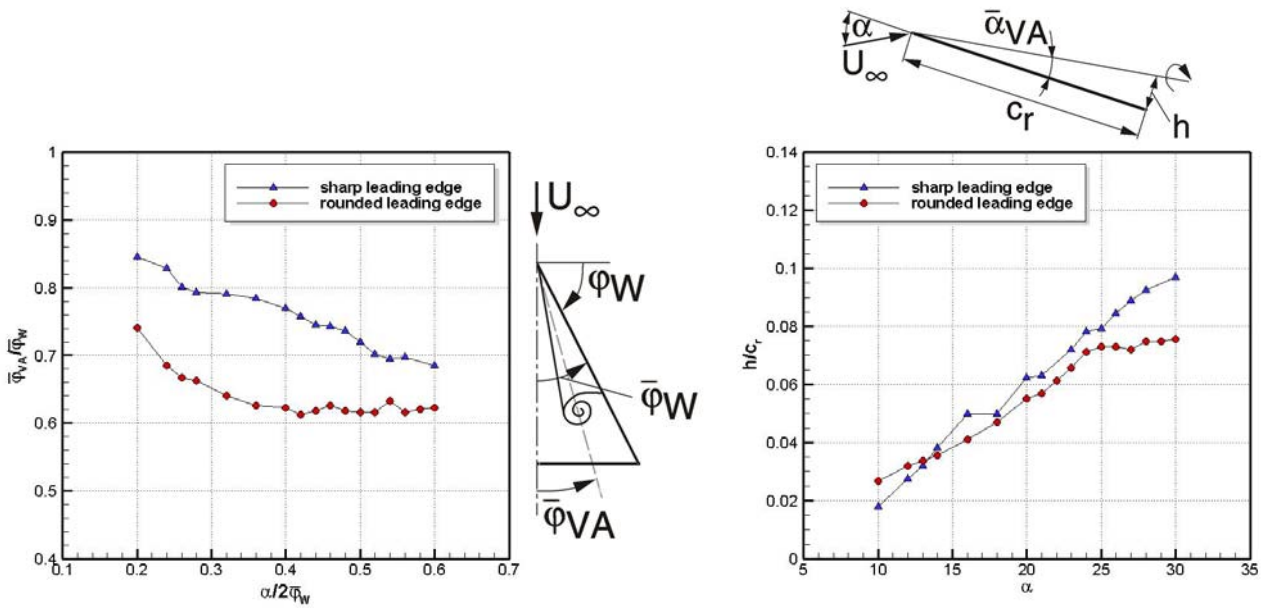

(a) Lateral Position (b) Vertical Position

Figure 21-9: Position of the Primary Vortex Axis at R_{mac} = 5 x 10^5 and M = 0.035 (Values Taken at x/c_r = 0.95).

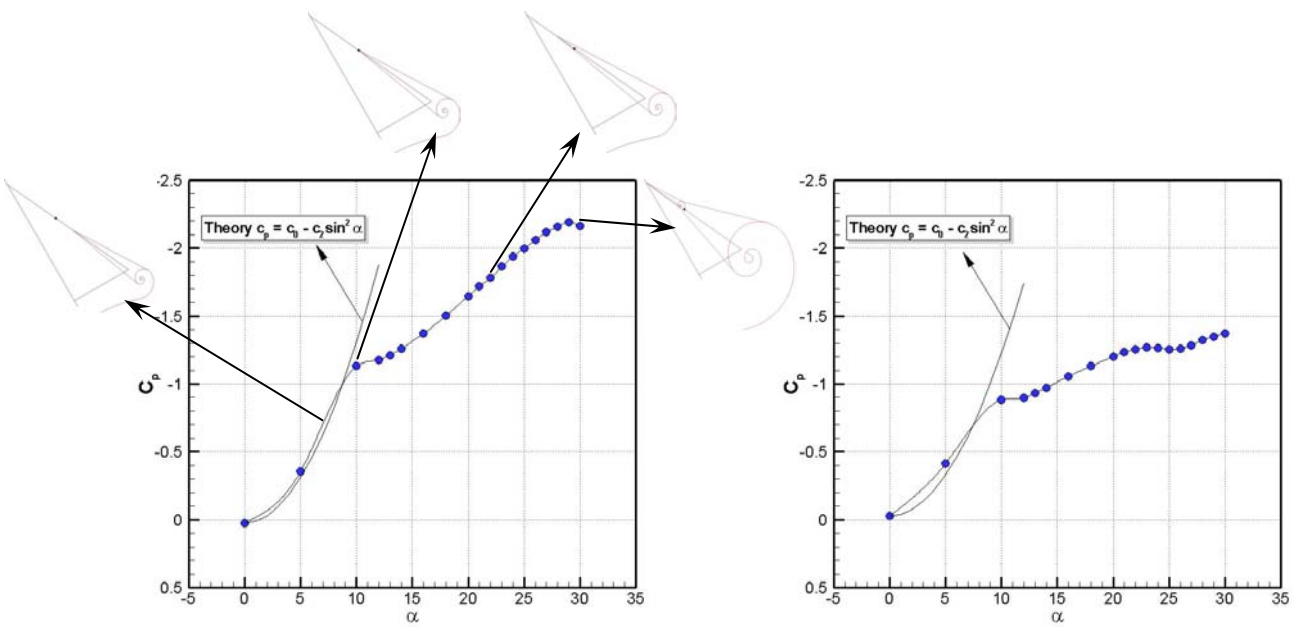

(a) Section x/c_r = 0.4 (b) Section x/c_r = 0.6

Figure 21-10: Correlation of Separation Onset with Leading Edge Steady Pressure Distribution for Sharp Leading Edge at R_{mac} = 2 x 10^6 in Position η = 0.95.

21.4.2.2 Velocity Distribution

The time-averaged velocities obtained by Stereo-PIV at cross sections x/c_r = 0.2, 0.4, 0.6, 0.8 and 0.95 (R_{mac} = 1 x 10^6, M = 0.07) are shown for an angle of attack of α = 18° in Figure 21-11 and Figure 21-12. The velocity components in axial direction are displayed as contour plots and in lateral and vertical direction as vector plots. For both sharp and rounded leading edges, fully developed leading-edge vortices are present. The structure of primary and secondary vortex is depicted by the corresponding increased cross flow velocity vectors.

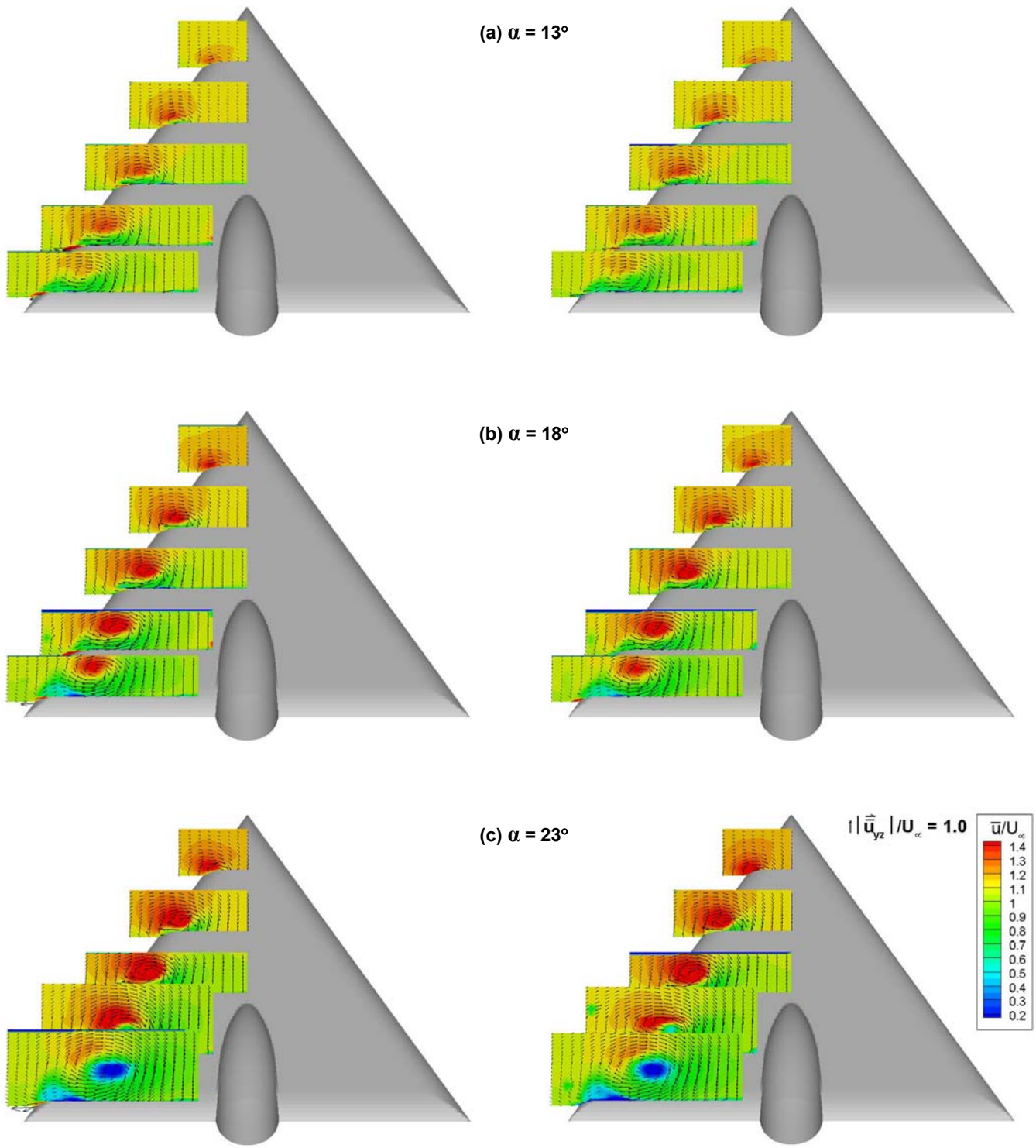

Figure 21-11: Mean Velocity Distribution at $R_{mac} = 1 \times 10^6$ and M = 0.07 for Sharp (left) and Rounded (right) Leading Edges.

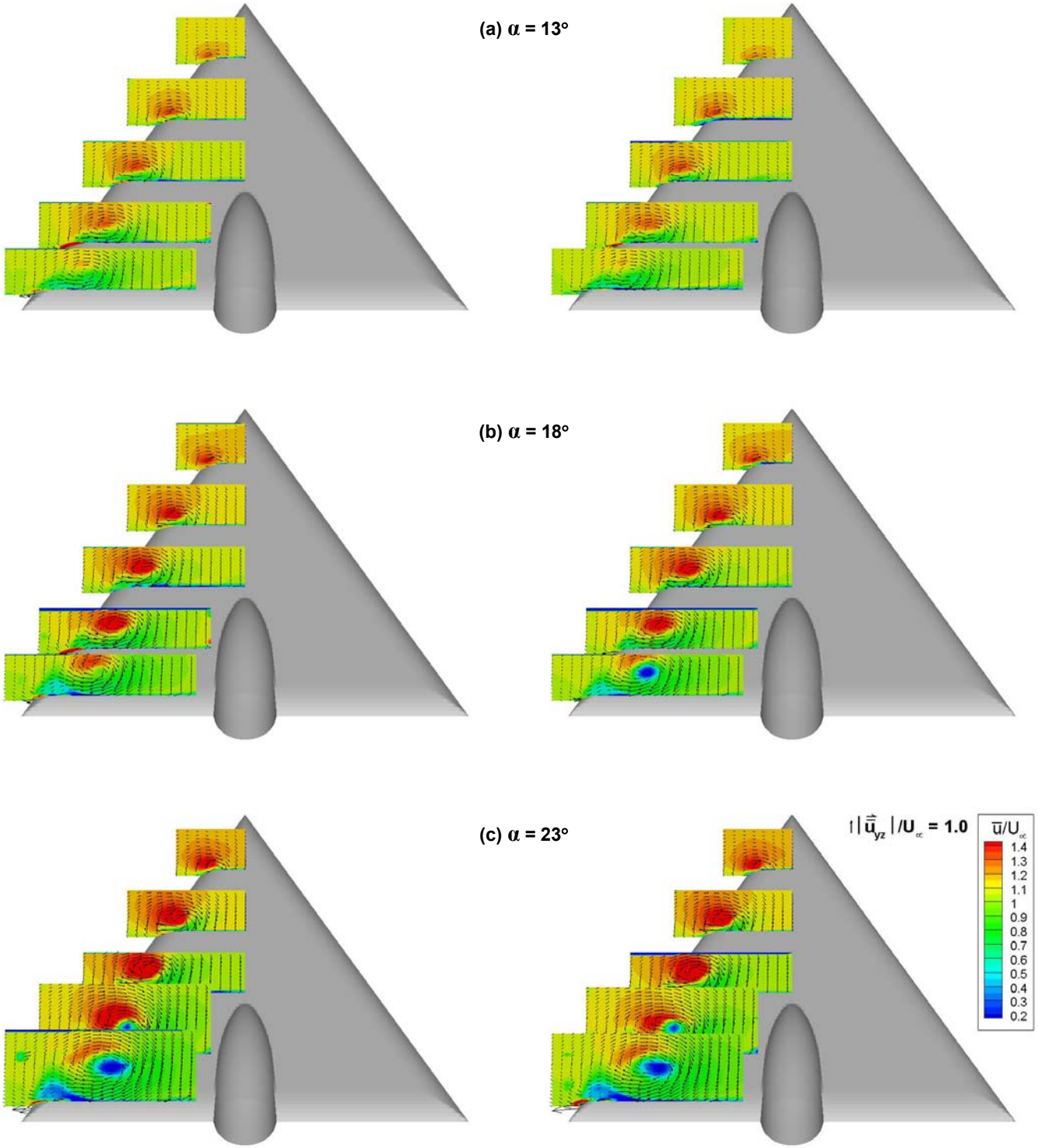

Figure 21-12: Mean Velocity Distribution at R_{mac} = 2 x 10^6 and M = 0.35 for Sharp (left) and Rounded (right) Leading Edges.

A comparison of the velocity fields obtained by Stereo-PIV and hot-wire anemometry for $\alpha = 18°$ and $x/c_r = 0.6$ shows that the corresponding contour lines of all three velocity components, u, v, w, correspond very well, Figure 21-13. The primary vortex is associated with axial accelerated flow, with an axial peak velocity of $\overline{u}/U_\infty = 1.6$ for both sharp and rounded leading-edge [21-14]. The wing inboard region is characterized by attached flow while there is no clear indication for a small inboard vortex by this mean velocity field. The overall flowfield pattern does not show markable differences between the configurations of sharp and rounded leading-edge.

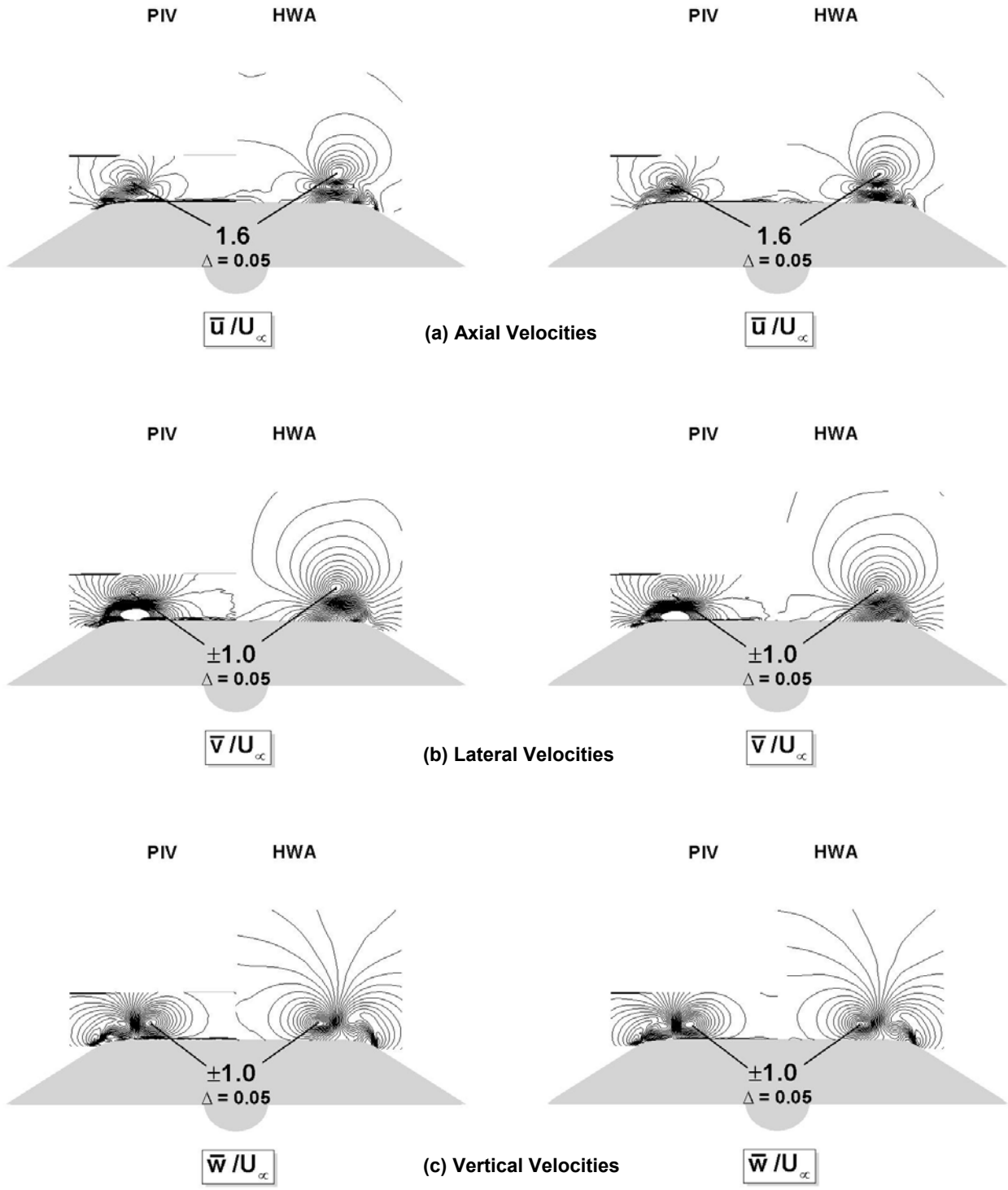

Figure 21-13: Comparison between Stereo-PIV and HWA Results for α = 18° at R_{mac} = 1 x 10^6 and M = 0.07 for Sharp (left) and Rounded (right) Leading Edge in Section x/c_r = 0.6.

21.4.3 Turbulent Flow Field

21.4.3.1 Unsteady Surface Pressure Intensities

The fluctuation part of the pressure coefficient $c'_p(P,t)$ is described by:

$$c'_p(P,t) = c_p(P,t) - \bar{c}_p(P) \ . \tag{3}$$

The mean square value of the pressure coefficient $\overline{c'^2_p}(P)$ is therefore:

$$\overline{c'^2_p}(P) = \frac{1}{t_M}\int_0^{t_M}[c_p(P,t) - \bar{c}_p(P)]^2\,dt \ . \tag{4}$$

The root mean square value is denoted rms-value $c_{p_{rms}}(P)$:

$$c_{p_{rms}}(P) = \sqrt{\overline{c'^2_p}(P)} \tag{5}$$

Referring again to angles of attack of α = 13°, α = 18° and α = 23°, the unsteady surface pressures are discussed based on root-mean-square (rms) values of the pressure coefficient and pressure amplitude spectra. The maximum peak of pressure fluctuation intensities C_{prms} in section $x/c_r = 0.6$ is observed in the area of the primary vortex outside of the suction peak near the attachment line of the secondary vortex (Figure 21-14 and Figure 21-15). The suction peak of the mean pressure $\bar{c}_p$ is broadened for the case of rounded leading-edge. It is located closer to the leading-edge due to retarded primary separation in comparison to the sharp leading-edge. The primary separation line, which is not geometrically fixed for the rounded leading-edge, is associated with increased pressure fluctuation intensities in the area of the leading edge η = 0.8 ÷ 1 in comparison to the sharp edge case.

(a) α = 13°

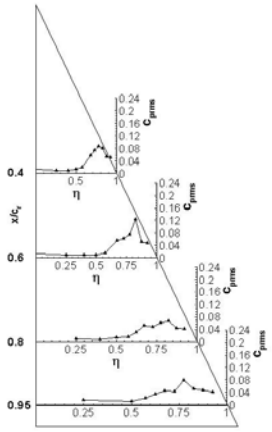

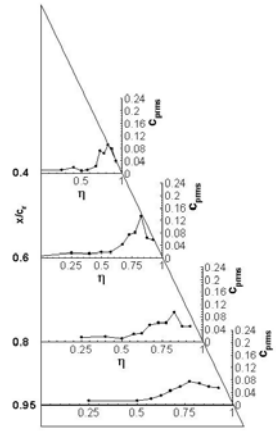

(b) α = 18°

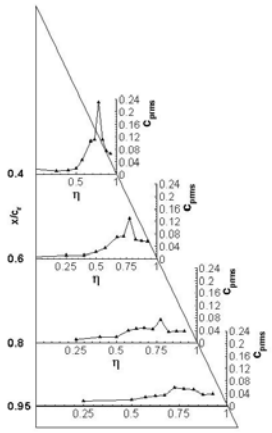

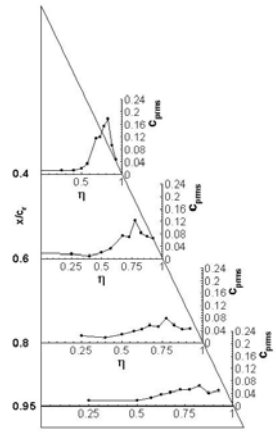

(c) α = 23°

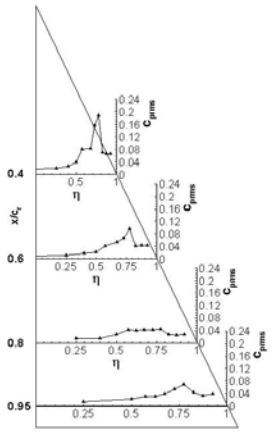

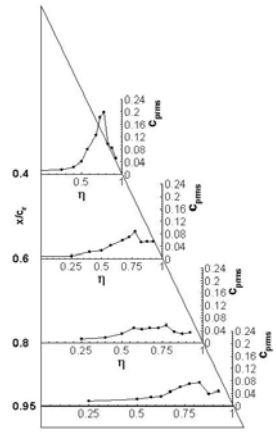

Figure 21-14: Pressure Fluctuation Intensity at R_{mac} = 1 x 10^6 and M = 0.07 for Sharp (left) and Rounded (right) Leading Edges.

(a) α = 13°

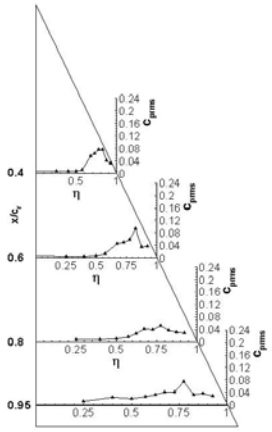

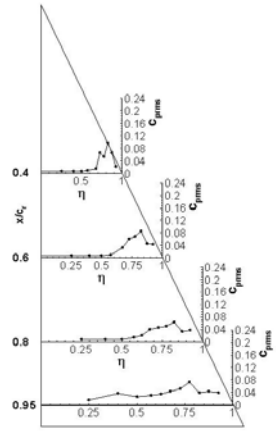

(b) α = 18°

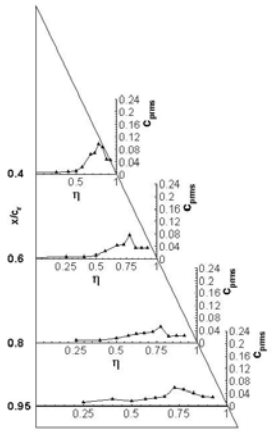

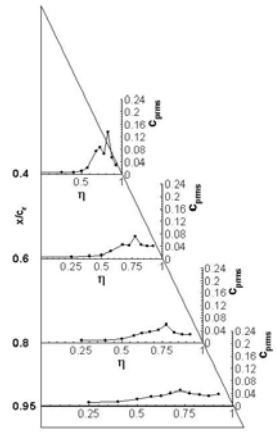

(c) α = 23°

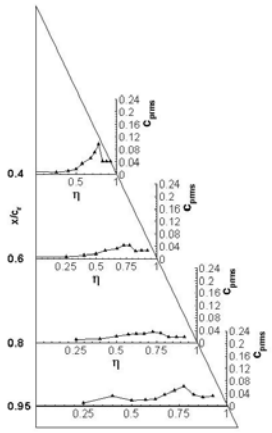

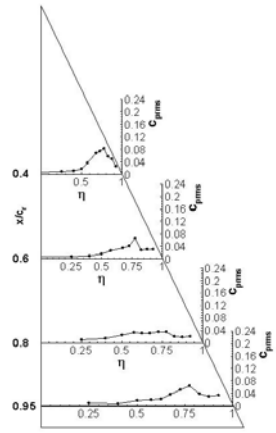

Figure 21-15: Pressure Fluctuation Intensity at R_{mac} = 2 x 10^6 and M = 0.14 for Sharp (left) and Rounded (right) Leading Edges.

21.4.3.2 Unsteady Surface Pressure Spectra

The fluctuation part p'(P,t) of the discrete time function p(P,t), respectively is Fourier transformed based on the relation:

$$X_p(P,\omega) = \lim_{t_M \to \infty} \int_0^{t_M} p'(P,t) e^{-i\omega t} dt \ . \tag{6}$$

The multiplication of the Fourier transformed quantities $X_p(P,\omega)$ with its conjugated complex quantities $X_p^*(P,\omega)$ leads to the power spectral density function.

$$S_P(P,\omega) = \lim_{t_M \to \infty} \frac{2}{t_M} X_p^*(P,\omega) X_p^T(P,\omega) \tag{7}$$

Accordingly, the power spectral density for the fluctuating part $S_{cp}(P,\omega)$ can be derived. The power spectral density of the pressure coefficient fluctuations still has the dimension of time. Taking into account the definition of the reduced frequency (Eq. 9) leads to the non dimensional power spectral density of the pressure coefficient fluctuations:

$$S_{c_p}^N(P,k) = \frac{U_\infty}{l_\mu} S_{c_p}(P,k) \tag{8}$$

$$k = \frac{f \cdot \bar{c}}{U_\infty} \tag{9}$$

The non dimensional power spectral density of the pressure coefficient $S_{c_p}^N$(P,k) can be transformed to an amplitude spectrum of the pressure coefficient:

$$\hat{c}_p(P,k) = \sqrt{2 S_{c_p}^N(P,k) \Delta k} \tag{10}$$

The amplitude spectra of the fluctuating pressure coefficient $\hat{c}_p$ are plotted as function of reduced frequency k for each measured spanwise station η for α = 13°, 18°, and 23° in Figure 21-16, Figure 21-17, and Figure 21-18. At an angle of attack of α = 13°, the amplitude level of pressure spectra for the rounded leading edge is slightly higher as for the sharp leading edge, especially in the low frequency domain, Figure 21-16. By increasing the angle of attack to α = 18° no significant change is noticeable, except for the amplitude spectrum at x/c_r = 0.4 for the rounded leading edge, Figure 21-17. There, the level of the highest frequencies is clearly increased and reaches a maximum $\hat{c}_p$ = 0.012 in the range of k = 2 ÷ 3.1, which illustrates the separation of the secondary vortex. Raised amplitude values can be detected in direction to the leading-edge linked to fluctuations in the primary separation and secondary separation and attachment. The spectra reveal a broadband behavior and are typical for a fully developed leading-edge primary vortex [[21-1], [21-2], [21-11], [21-12]].

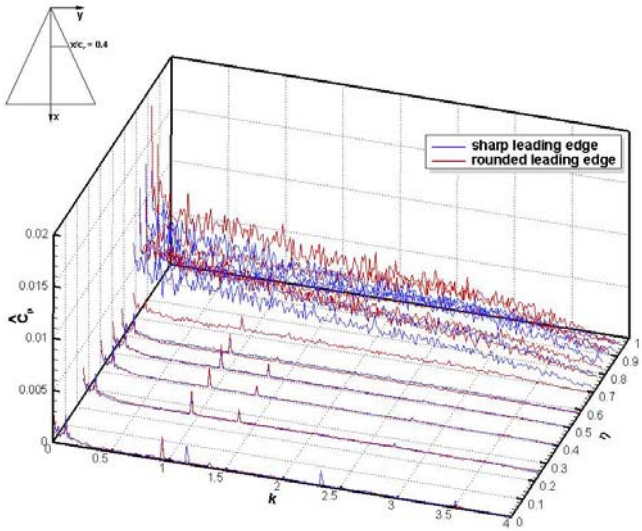

(a) $x/c_r = 0.4$

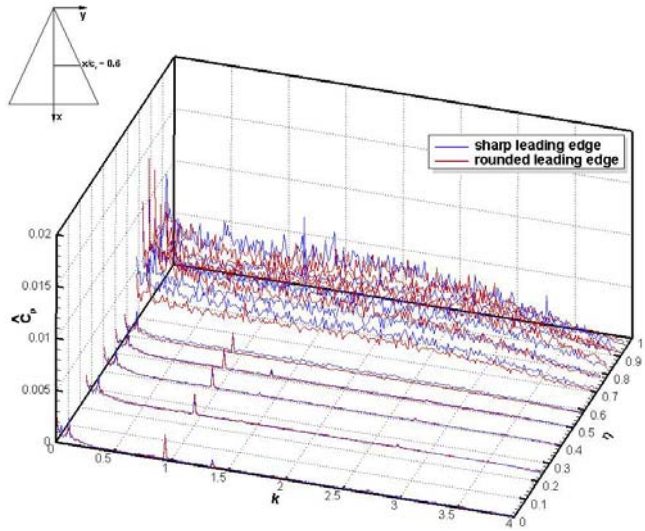

(b) $x/c_r = 0.6$

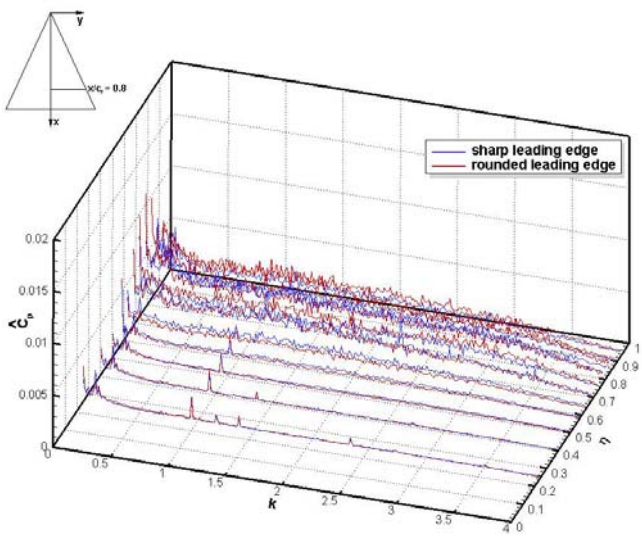

(c) $x/c_r = 0.8$

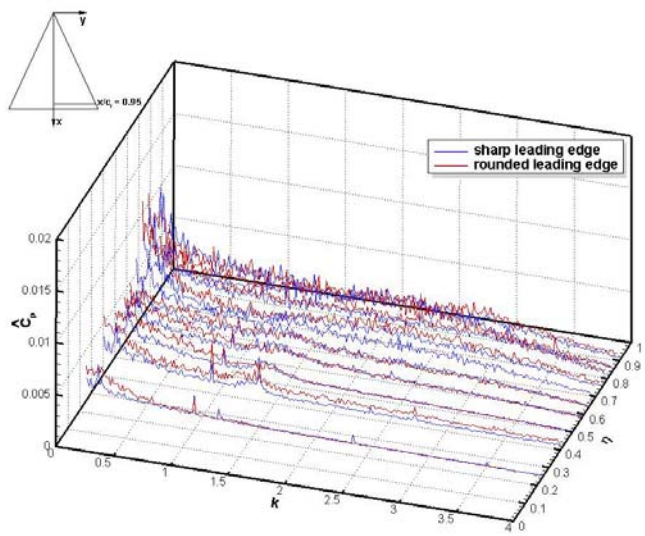

(d) $x/c_r = 0.95$

Figure 21-16: Amplitude Spectra of Fluctuating Pressure Coefficient for Sharp and Rounded Leading Edge at $\alpha = 13°$, $R_{mac} = 2 \times 10^6$ and M = 0.14.

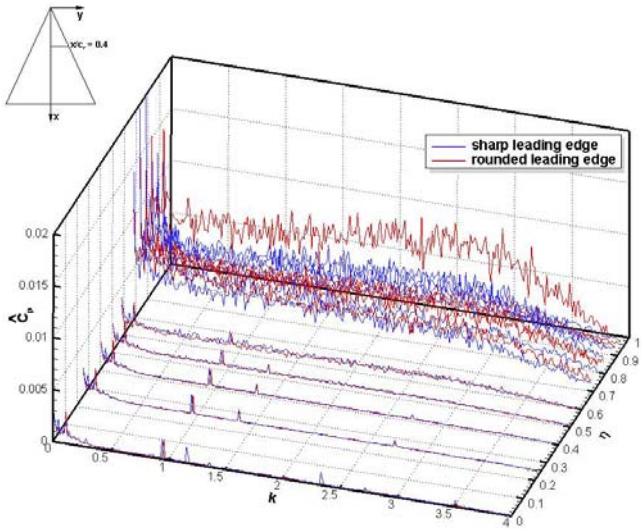

(a) $x/c_r = 0.4$

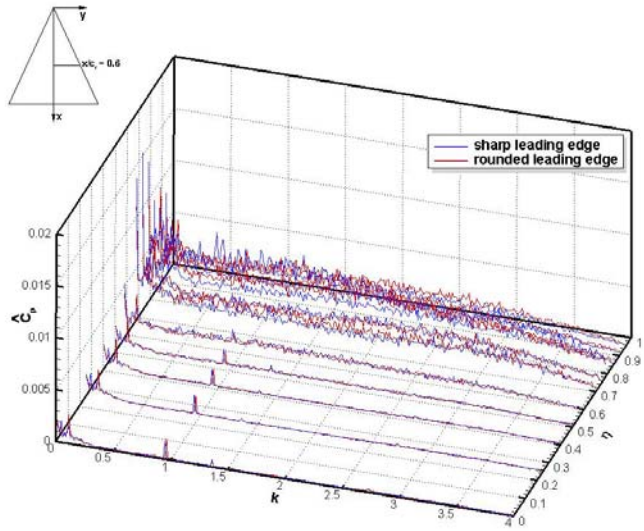

(b) $x/c_r = 0.6$

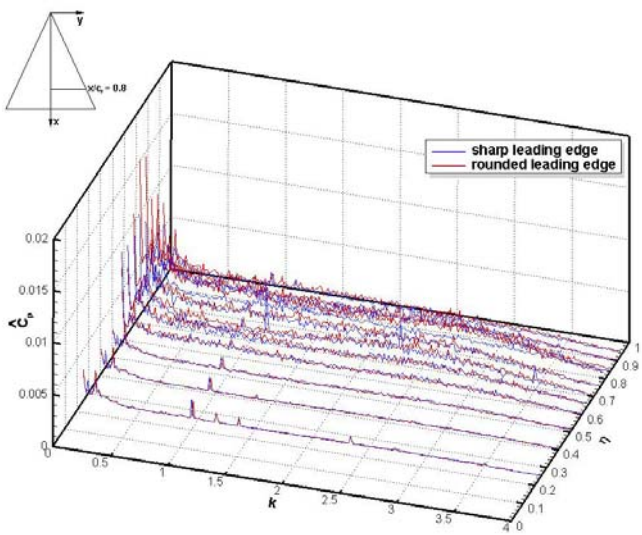

(c) $x/c_r = 0.8$

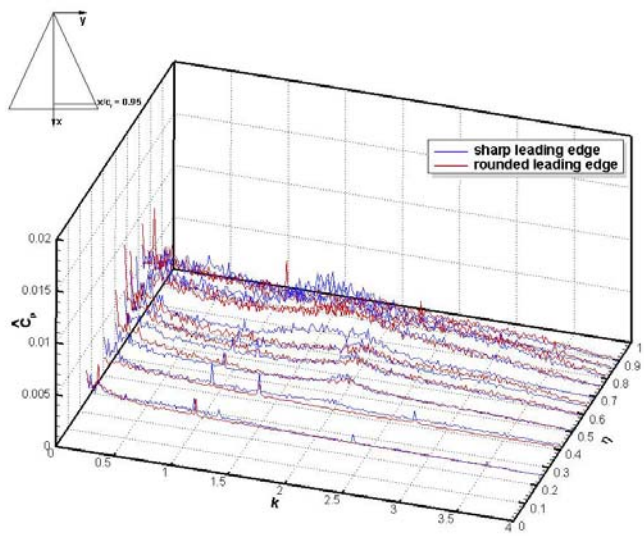

(d) $x/c_r = 0.95$

Figure 21-17: Amplitude Spectra of Fluctuating Pressure Coefficient for Sharp and Rounded Leading Edge at α = 18°, $R_{mac} = 2 \times 10^6$ and M = 0.14.

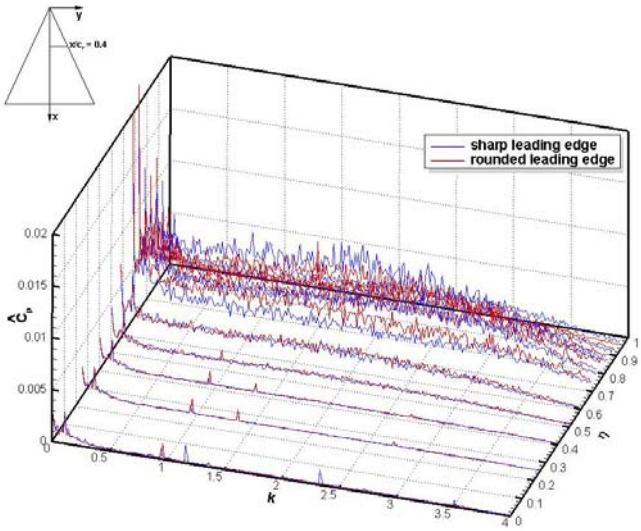

(a) $x/c_r = 0.4$

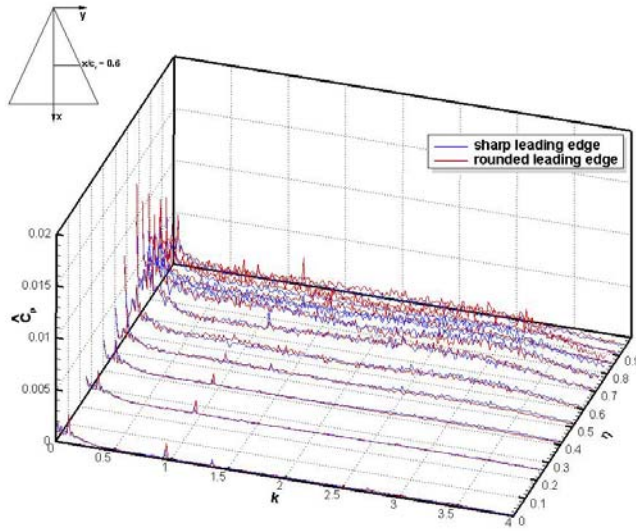

(b) $x/c_r = 0.6$

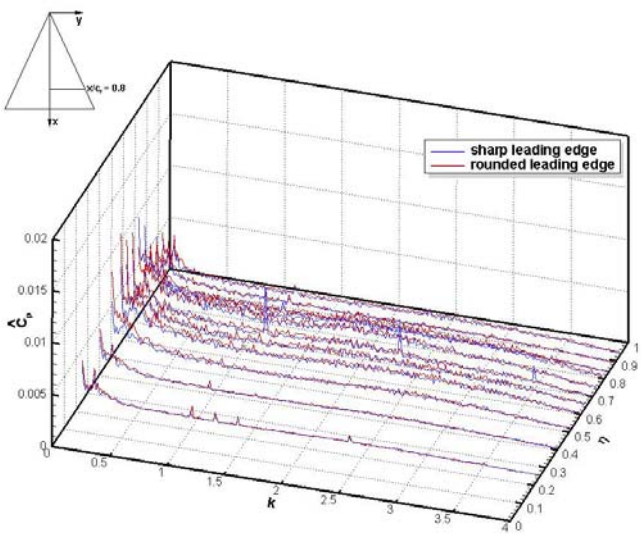

(c) $x/c_r = 0.8$

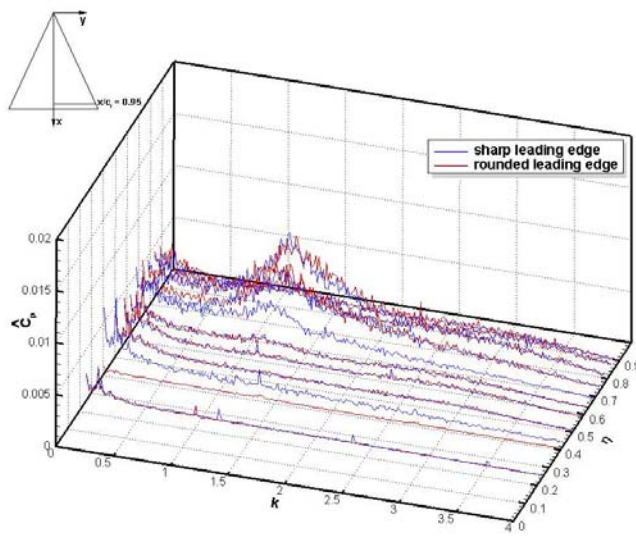

(d) $x/c_r = 0.95$

Figure 21-18: Amplitude Spectra of Fluctuating Pressure Coefficient for Sharp and Rounded Leading Edge at α = 23°, $R_{mac} = 2 \times 10^6$ and M = 0.14.

At an angle of attack of α = 23°, the increase in amplitude for both leading-edge geometries is visible, whereby the increase in the chord station $x/c_r = 0.4$ for the sharp leading-edge is more significant, Figure 21-18. The increase in the chord station $x/c_r = 0.95$, especially the amplitude peaks $\hat{c}_p = 0.0095$ at k = 1.1 ÷ 1.4, indicate the breakdown of the primary vortex for both leading-edge geometries. This takes place for the rounded

leading at η = 0.775 and for the sharp leading edge at η = 0.825. An additional increase in the high frequency domain (k = 2.5 ÷ 3.0) to $\hat{c}_p$ = 0.005 illustrates the separation at the trailing edge.

21.4.3.3 Velocity Fluctuation Intensities and Reynolds Stresses

For each flowfield position P the time series of the velocities u_i(P,t) are available for every test condition.

The average of the velocity $\overline{u}_i$ (P,t) is defined as:

$$\overline{u}_i(P) = \frac{1}{t_M}\int_0^{t_M} u_i(P,t)dt \ , \tag{11}$$

with t_M as the measurement time or length of the time series. The fluctuation part of the velocity u_i'(P,t) is described by:

$$u_i'(P,t) = u_i(P,t) - \overline{u}_i(P) \ . \tag{12}$$

The mean square value of the velocity fluctuations $\overline{u_i'^2}(P)$ is therefore:

$$\overline{u_i'^2}(P) = \frac{1}{t_M}\int_0^{t_M} [u_i(P,t) - \overline{u}_i(p)]^2 dt \ . \tag{13}$$

The root mean square value is denoted rms-value $u_{i_{rms}}$ (P) and is converted in non-dimensional values:

$$\frac{u_{i_{rms}}(P)}{U_\infty} = \frac{\sqrt{\overline{u_i'^2}(P)}}{U_\infty} \tag{14}$$

The fluctuating velocity field at station x/c_r = 0.4, x/c_r = 0.6 and x/c_r = 0.8 for α = 13°, 18°, and, 23° is obtained by hot-wire measurements, the results of which are shown for sharp and rounded leading-edge in Figure 21-19 – Figure 21-23. In Figure 21-19, the rms values of the axial velocity fluctuations are plotted. The fluctuation intensities indicate high levels for the viscous core of the primary vortex and the region of the secondary vortex and moderate levels for the separating shear layer and primary vortex rotational core. The intensity of the lateral velocity fluctuations also displays high levels for the primary vortex subcore as well as for the shear layer, Figure 21-20. Considering the intensity of the vertical velocity fluctuations, increased values exist mainly in the primary vortex subcore, Figure 21-21. Moderate levels are found for the region of the secondary vortex because the vertical velocity fluctuations are the first to be damped approaching the wing surface. The shear stress $\overline{u'v'}/U_\infty{}^2$ shows high positive values in the vortex core and in the surface flow under the primary vortex, Figure 21-22. High negative values are visible in the region of the outboard shear layer and in the shear layer over the primary vortex subcore. Negative and positive values are determined by the direction of the lateral velocity when moving from outboard to inboard along the vorticity feeding shear layer. The shear stress distribution $\overline{u'w'}/U_\infty{}^2$ exhibit again increased levels for the regions of

vertical flow, Figure 21-23. Peak values are located in neighboured regions relative to the $\overline{u'v'}$-maxima and are of opposite sign. The direction of the vertical velocity determines the sign of this stress component.

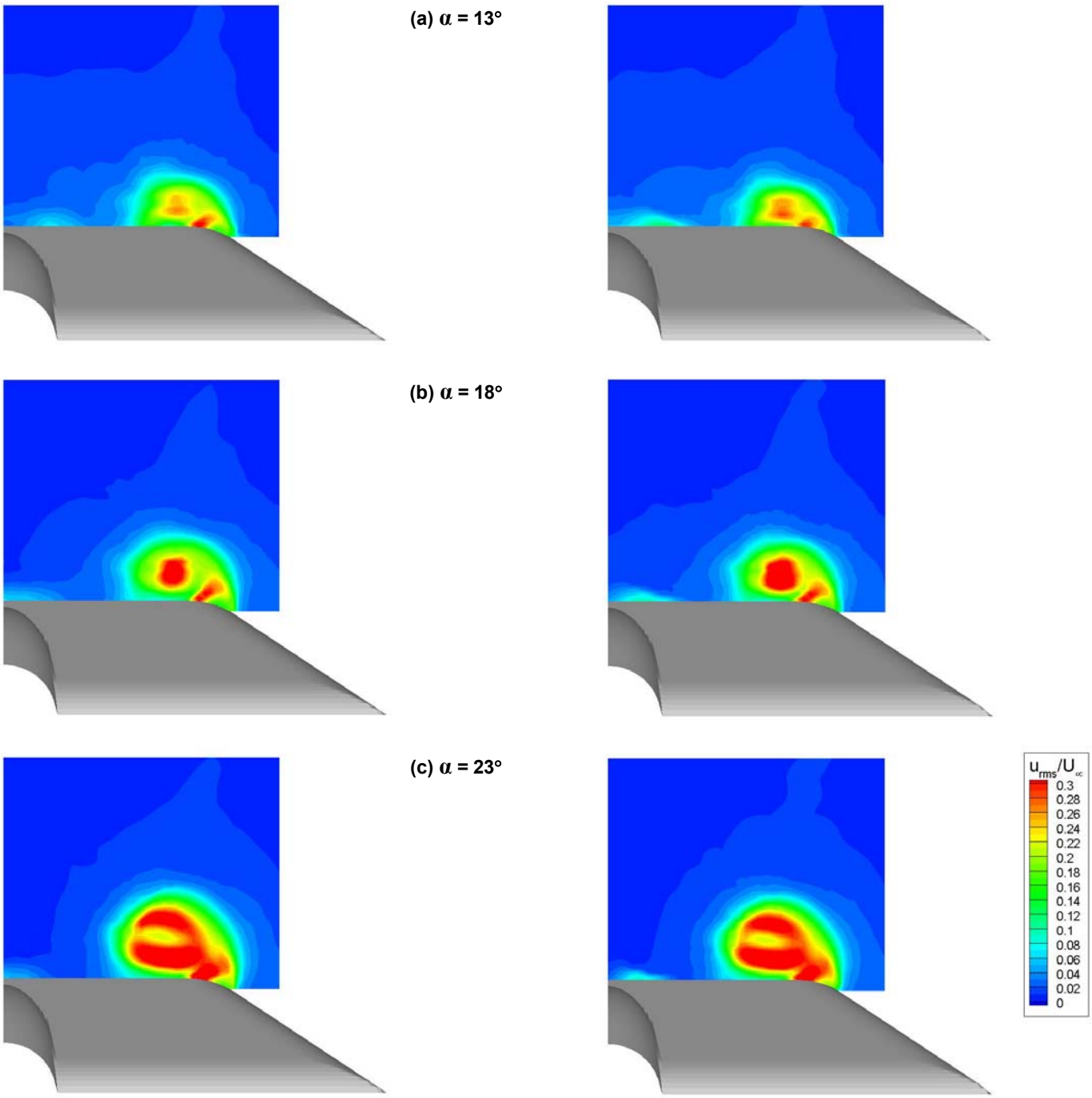

Figure 21-19: Turbulence Intensity Distribution of the Axial Velocity Fluctuations at R_{mac} = 1 x 10^6 and M = 0.07 for Sharp (left) and Rounded (right) Leading Edge in Section x/c_r = 0.6.

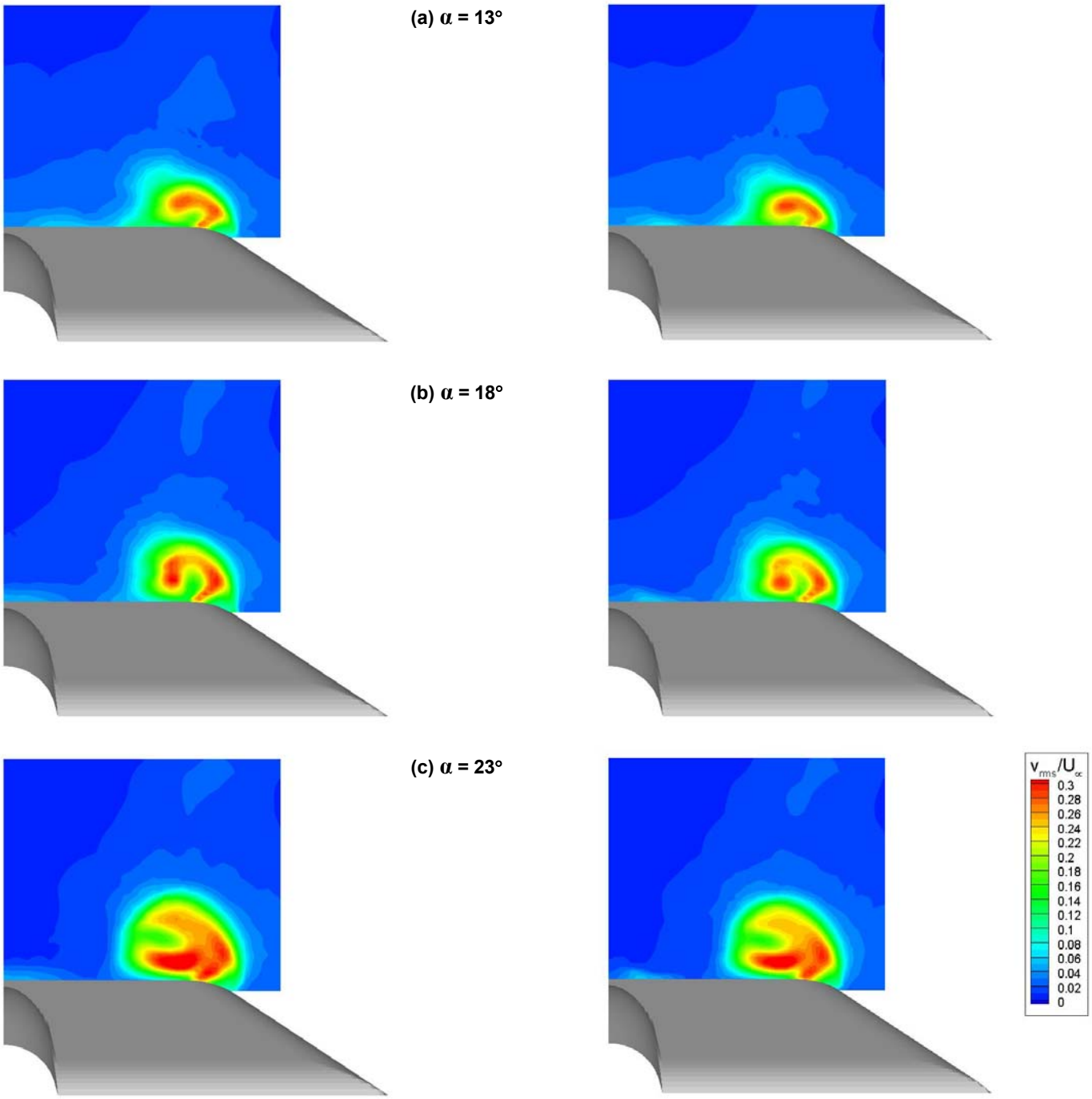

Figure 21-20: Turbulence Intensity Distribution of the Lateral Velocity Fluctuations at R_{mac} = 1 x 10^6 and M = 0.07 for Sharp (left) and Rounded (right) Leading Edge in Section x/c_r = 0.6.

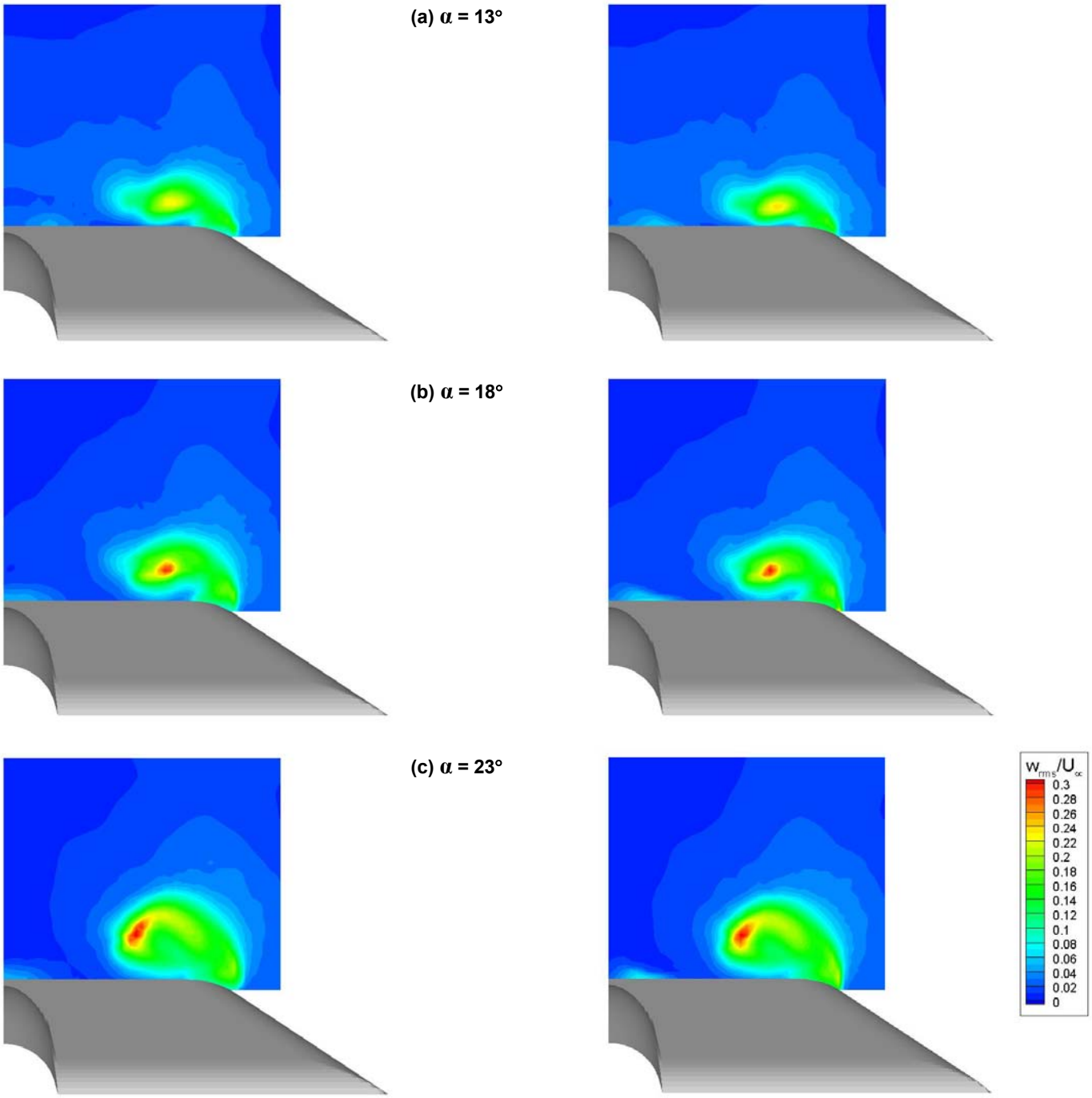

Figure 21-21: Turbulence Intensity Distribution of the Vertical Velocity Fluctuations at R_{mac} = 1 x 10^6 and M = 0.07 for Sharp (left) and Rounded (right) Leading Edge in Section x/c_r = 0.6.

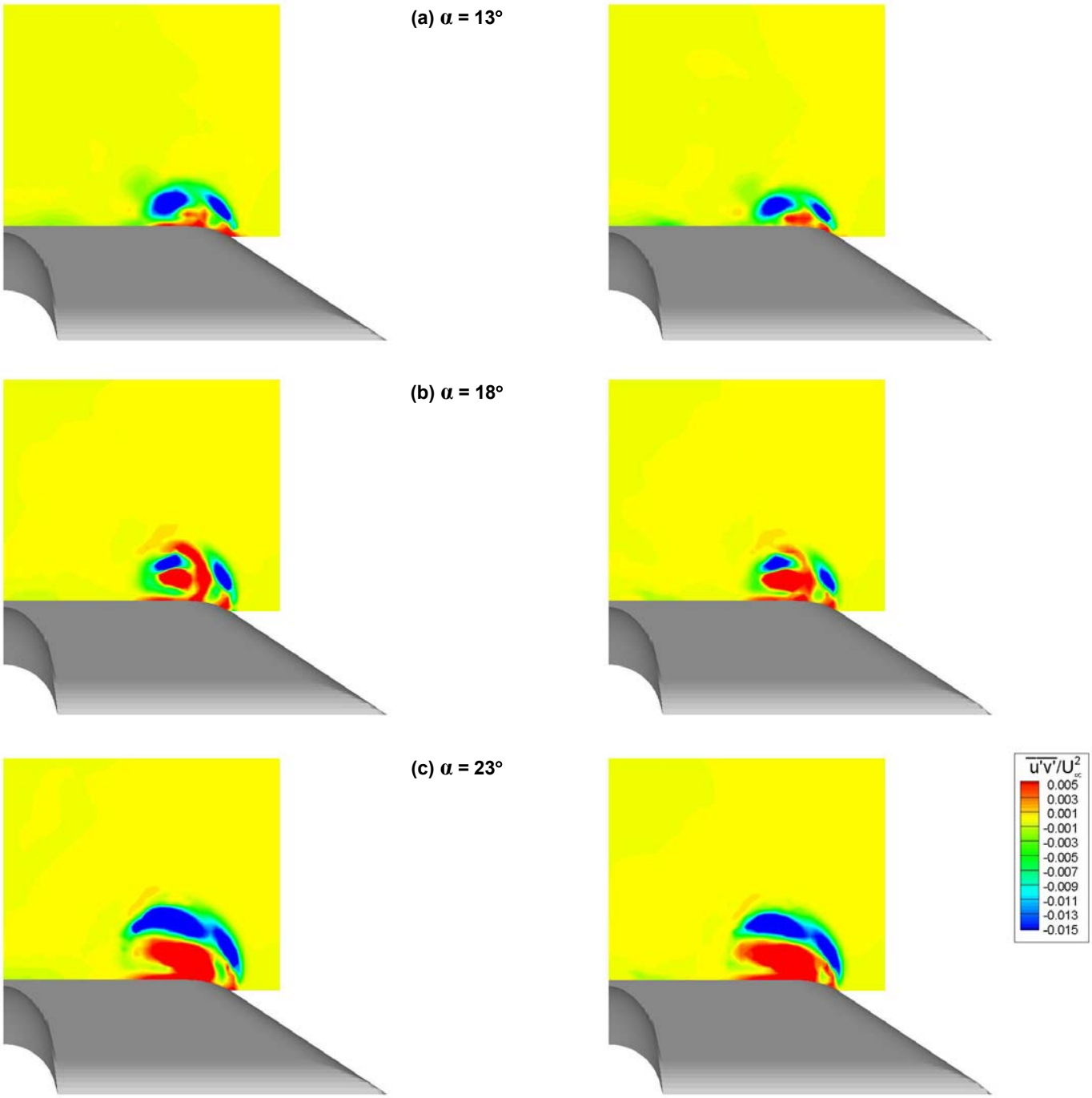

Figure 21-22: Shear Stress Distribution of the Axial and Lateral Velocity Fluctuations at R_{mac} = 1 x 10^6 and M = 0.07 for Sharp (left) and Rounded (right) Leading Edge in Section x/c_r = 0.6.

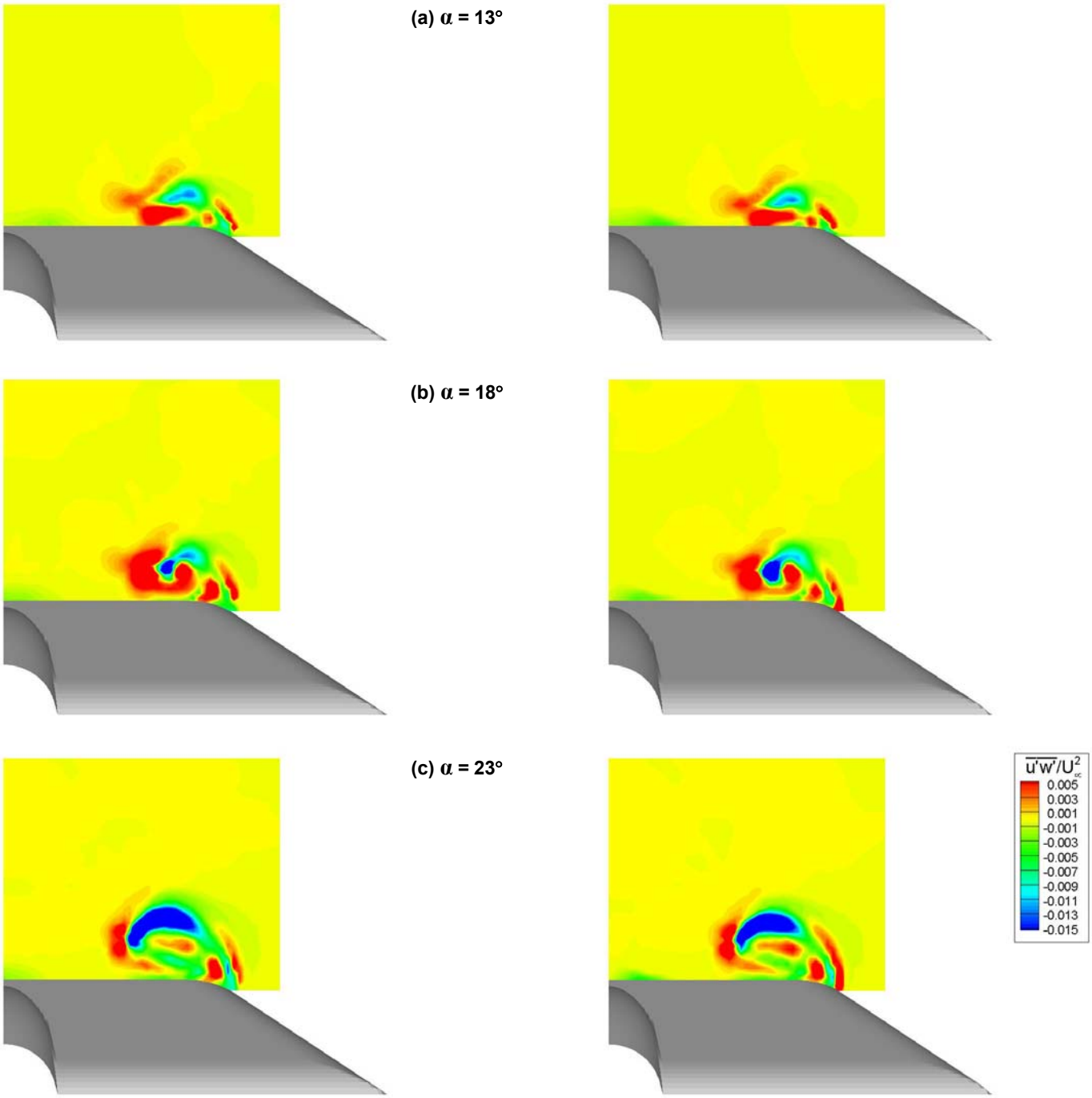

Figure 21-23: Shear Stress Distribution of the Axial and Vertical Velocity Fluctuations at R_{mac} = 1 x 10^6 and M = 0.07 for Sharp (left) and Rounded (right) Leading Edge in Section x/c_r = 0.6.

A small region of slightly increased velocity fluctuations and turbulent shear stresses near the symmetry plane of the wing is due to the weak inboard vortex, the development of which was explained above.

21.4.3.4 Spectral Densities of Velocity Fluctuations

Spectral analysis is applied to the velocity time series to study the characteristics in the area of the highest velocity fluctuation intensity. The fluctuation part u_i'(P,t) of the discrete time function u_i (P,t) is Fourier transformed based on the relation:

$$X_{u_i'}(P,\omega) = \lim_{t_M \to \infty} \int_0^{t_M} u_i'(P,t) e^{-i\omega t} dt \ . \tag{15}$$

The multiplication of the Fourier transformed quantity $X_{u_i'}(P,\omega)$ with its conjugated complex quantity $X_{u_i'}^*(P,\omega)$ leads to the power spectral density function:

$$S_{u_i'}(P,\omega) = \lim_{t_M \to \infty} \frac{2}{t_M} X_{u_i'}^*(P,\omega) X_{u_i'}^T(P,\omega) \ . \tag{16}$$

The power spectral density of the velocity fluctuations has the dimension of the square of velocity and time. Taking into account the definition of the reduced frequency leads to the non dimensional power spectral density of the velocity fluctuations:

$$S_{u_i'}^N(P,k) = \frac{U_\infty}{\bar{c} u_i'^2} S_{u_i'}(P,k) \tag{17}$$

The power spectral density distributions of the axial velocity fluctuations are shown for a number of measurement points crossing laterally through the vortex core region and the separating shear layer. The angles of attack discussed include α = 18° and 23°. The measurement stations are depicted in Figure 21-24, Figure 21-25, Figure 21-26 and Figure 21-27 (left) for the three cross sections of interest, namely x/c_r = 0.4, 0.6 and 0.8, with respect to the contour lines of the turbulence intensity distributions of the axial velocity fluctuations. The corresponding power spectral density distributions are plotted in Figure 21-24 – Figure 21-27 (right).

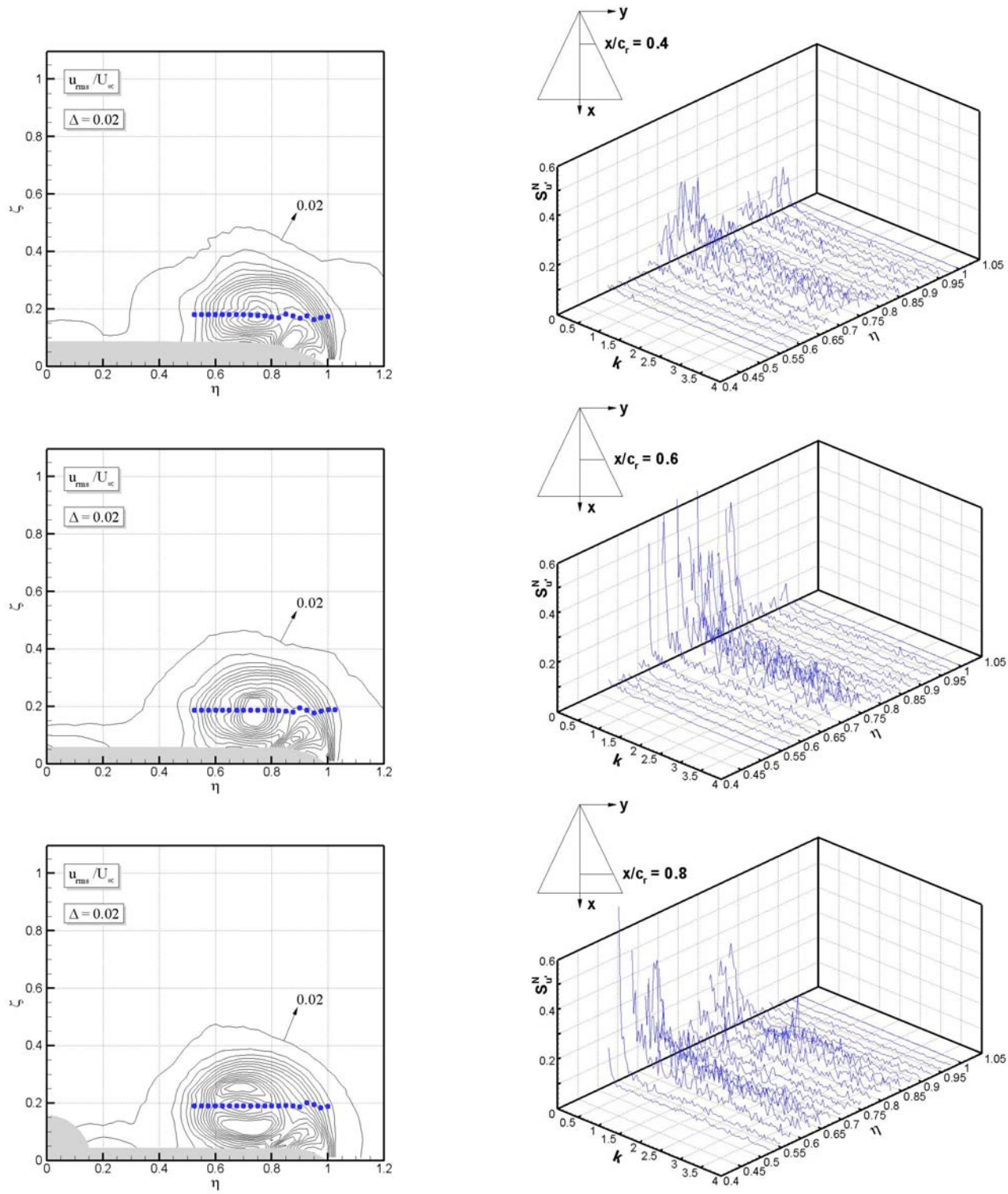

Figure 21-24: Power Spectral Density Distributions of the Axial Velocity Fluctuations at α = 18°, R_{mac} = 1 x 10^6 and M = 0.07 for Sharp Leading Edge.

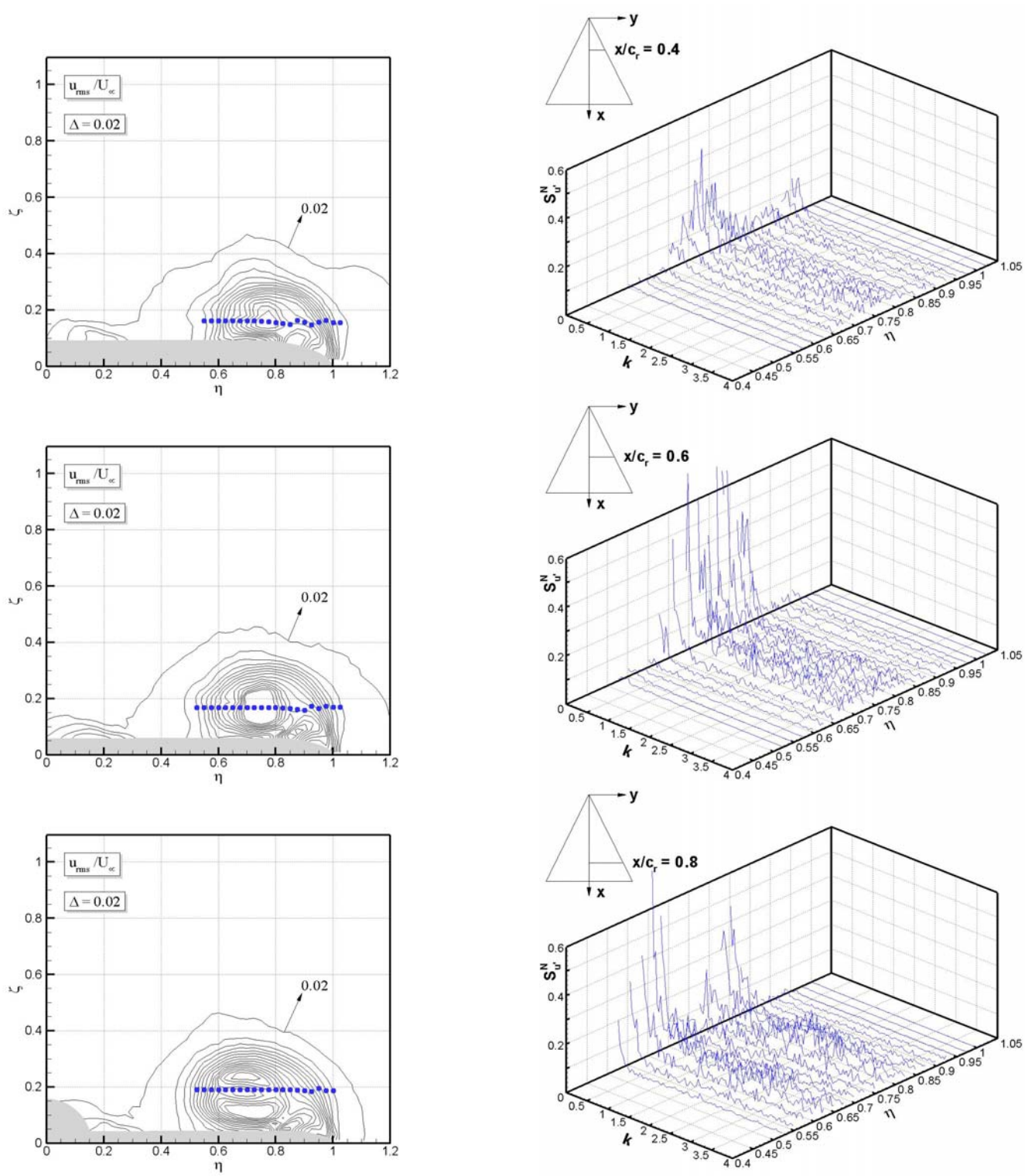

Figure 21-25: Power Spectral Density Distributions of the Axial Velocity Fluctuations at α = 18°, R_{mac} = 1 x 10^6 and M = 0.07 for Rounded Leading Edge.

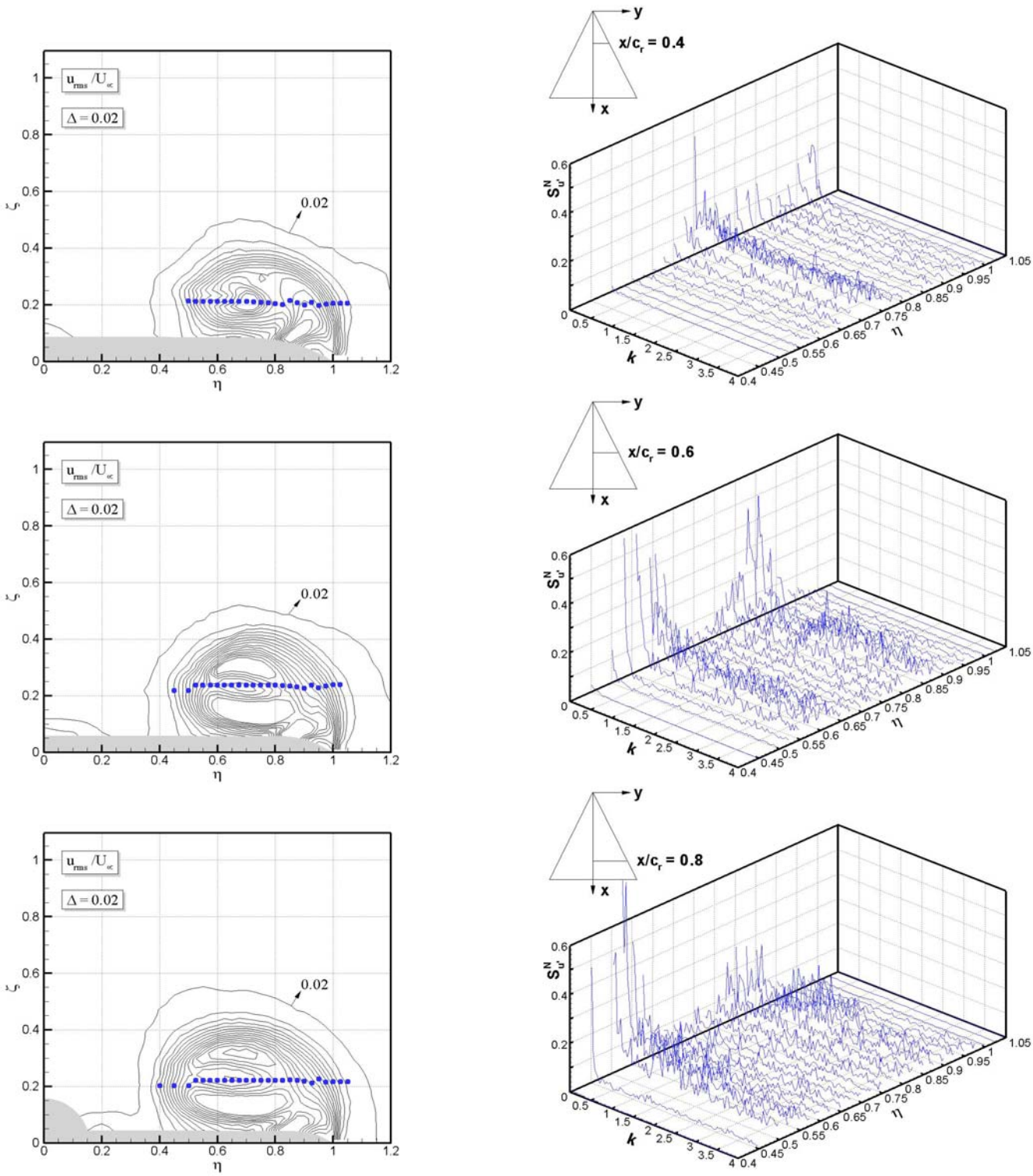

Figure 21-26: Power Spectral Density Distributions of the Axial Velocity Fluctuations at α = 23°, R_{mac} = 1 x 10^6 and M = 0.07 for Sharp Leading Edge.

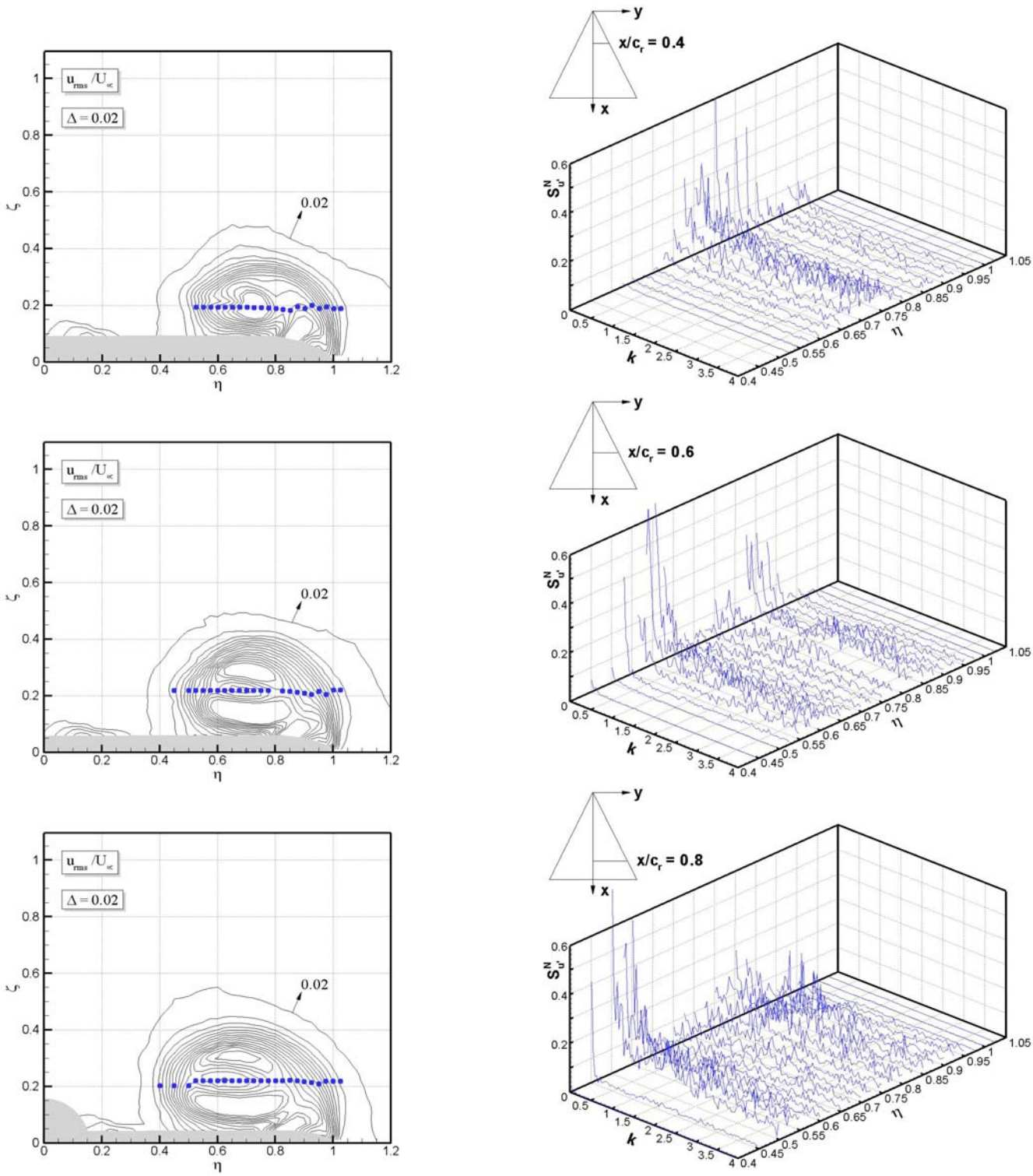

Figure 21-27: Power Spectral Density Distributions of the Axial Velocity Fluctuations at α = 23°, R_{mac} = 1 x 10^6 and M = 0.07 for Rounded Leading Edge.

Considering the fully developed leading-edge vortex at $\alpha = 18°$ and $x/c_r = 0.4$, the power spectral densities exhibit increased values within the vortex core region and the rolled up shear layer, Figure 21-24 (a), Figure 21-25 (a). Some energy overshoots are present in the low frequency range. At $x/c_r = 0.6$, the power spectral densities of the core region increases revealing again some high peaks at lower frequencies, Figure 21-24 (b), Figure 21-25 (b). Downstream of vortex breakdown, $x/c_r = 0.8$, the power spectral densities exhibit increased levels in two laterally separated areas matching with the annular structure detected for the turbulence intensity distribution, Figure 21-24 (c), Figure 21-25 (c). Beside the spectral peaks in the low frequency range there is also a certain increase within a higher frequency range attributed to the helical mode instability of the breakdown flow. This instability results from the wake-type swirling flow in the breakdown region, Figure 21-26, Figure 21-27.

21.4.3.5 Vortex Bursting and Dominant Frequency

With increasing angle of attack vortex bursting occurs over the wing as shown by the turbulence intensity patterns and related spectral density distributions. Here, vortex breakdown takes place at $x/c_r = 0.75 \div 0.85$ for $\alpha = 23°$. The position of vortex breakdown can be determined by analyzing the surface pressure distribution [21-12]. If an increase in angle of attack does not cause an increase in the primary vortex suction peak comparing stations x/c_r = const., then the leading-edge vortex may experience breakdown. This criterion fails, if the primary vortex detaches from the wing surface and thereby reduces its influence on the pressure distribution at the same time, as the breakdown location passes the trailing-edge upstream. The detachment of the vortex axis for strong leading-edge vortices, present at this delta wing planform, is only observed at angles of attack beyond the ones investigated here. Therefore, the described breakdown criterion is applicable. This criterion can also be discussed in context of the turbulence intensity distributions, shown for the axial velocity fluctuations at $x/c_r = 0.8$. The turbulence intensity distribution exhibits an annular concentration of local rms maxima, Figure 21-19 (c). This turbulence structure is a characteristic feature of spiral vortex breakdown which is related to Reynolds numbers above 10^4 [[21-1], [21-13]].

The velocity and surface pressure fluctuations show increased spectral levels in the near wall flow with some narrow-band concentration within $k = 1 \div 2$ [21-14], Figure 21-28 (top). That means vortex breakdown has started to influence the surface pressure fluctuations. The narrow-band concentration of turbulent kinetic energy at burst flow conditions reflects the helical mode instability of the vortex breakdown flow [[21-14], [21-15]]. This impact may result in strong excitation of structural modes of an aircraft. The energy peak of the velocity fluctuations or pressure fluctuations, respectively, is called “buffet peak” It can be further detected that the reduced frequencies associated with the buffet peak, i.e. the dominant frequencies, are shifted to lower values with increasing angle of attack. The burst vortex core expands with increasing angle of attack and, therefore, the wavelength λ of the instability mode becomes larger and the corresponding frequency smaller, $f_{dom} \sim 1/\lambda \sim 1/(b_{loc}/2)$. A universal frequency parameter k_{dom} can be derived using appropriate scaling quantities, Figure 21-28. Referring to velocity, the component normal to the leading-edge ($U_\infty \sin\alpha$) has to be considered. The characteristic length scale l_C must account for the vortex core expansion of the burst leading-edge vortex given approximately by the local half span ($\sim (b_{loc}/2) = x \cot \varphi_W$) and the shear layer distance ($\sim \sin^2\alpha$). Thus, the following scaling relationship for the dominant reduced frequency is applied,

$$k_{dom} = \frac{f_{dom} \cdot x \cdot \cot\varphi_w}{U_\infty} \sin\alpha \quad , \tag{18}$$

resulting in a characteristic frequency range of 0.28 ± 0.05, derived in Ref. 1 for other delta wing geometries.

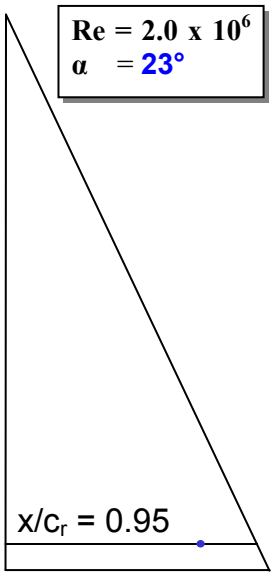

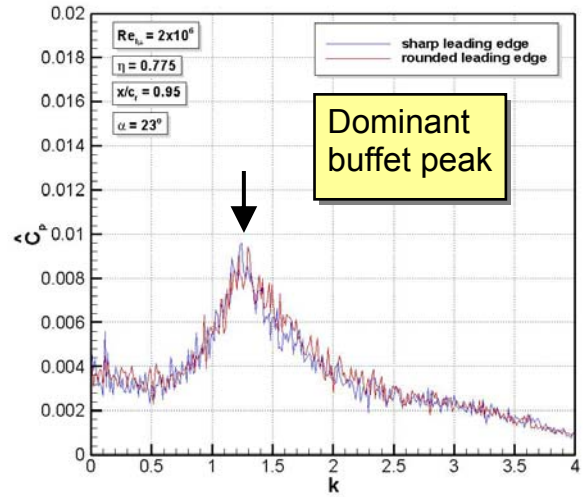

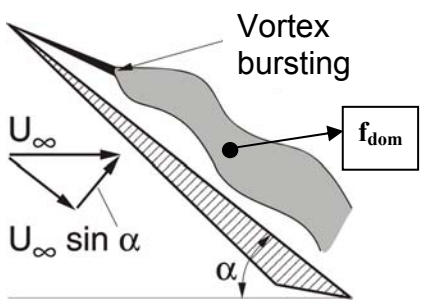

$$k_{dom} = \frac{f_{dom} \cdot l_c}{U_c}$$

$$U_c = U_\infty \cdot \sin\alpha$$

$$l_c = x \cdot \cot\varphi_w \cdot \sin^2\alpha$$

Frequency parameter:

$$k_{dom} \cdot \sin\alpha \cdot \cot\varphi_w \cong 0.28 \pm 0.05$$

Leading edge vortex breakdown flow

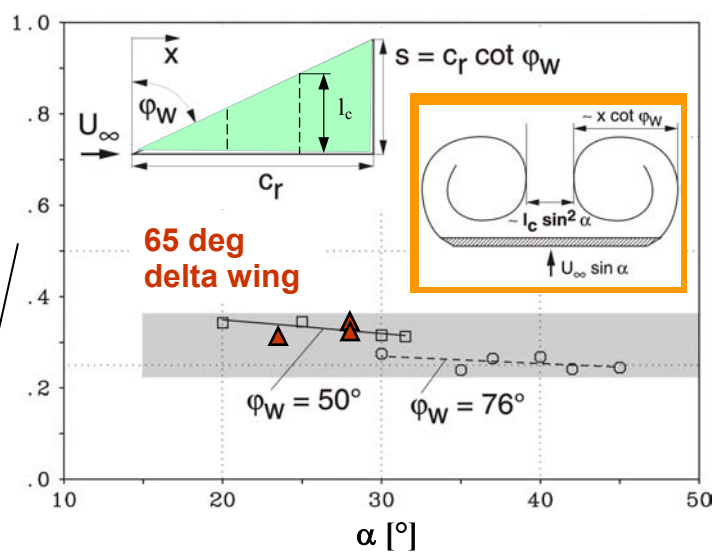

Scaling of the dominant reduced frequency k_{dom} with the local semi span ($x \cot \varphi_w$) and $\sin \alpha$

Figure 21-28: Dominant Reduced Frequency Correlation Based on Unsteady Surface Pressure (top) and Velocity Measurements [21-1].

21.4.4 Boundary Layer

Boundary layer profiles of mean axial velocity and velocity fluctuation components are discussed, regarding again the cases of α = 13°, 18°, and 23° and rounded leading-edge. The measurement points located closest to the wall were placed 1 mm above the wing surface. Figure 21-29 – Figure 21-34 top and bottom left show results for chord stations $x/c_r = 0.6$ and lateral positions of η = 0.4 and η = 0.6. The x-axis in the diagram represents the vertical distance from wing surface based on the local wing semi span $\varsigma = 2z/b_{loc}$. The left y-axis refers to the range of the mean axial velocity based on free stream velocity and the right y-axis refers to the range of the non-dimensional velocity fluctuations. The middle picture of Figure 21-29 – Figure 21-34 shows the oil flow image, with the measurement positions marked by red dots. The corresponding sections of surface pressure fluctuation intensities are also included (cf. Figure 21-14 right). Regarding the two chordwise stations, the profiles of the mean axial velocity indicate a turbulent boundary layer. All three rms velocities show significantly increased levels in the boundary layer and a low constant level outside. The same trend holds for the turbulent shear stresses which are multiplied by a factor of -20 for appropriate representation in the diagram. These turbulent boundary layers are typical for the wing inboard region close to the primary vortex attachment line. Only low surface pressure fluctuations are evoked as the flow is accelerated in direction to the vortex axis.

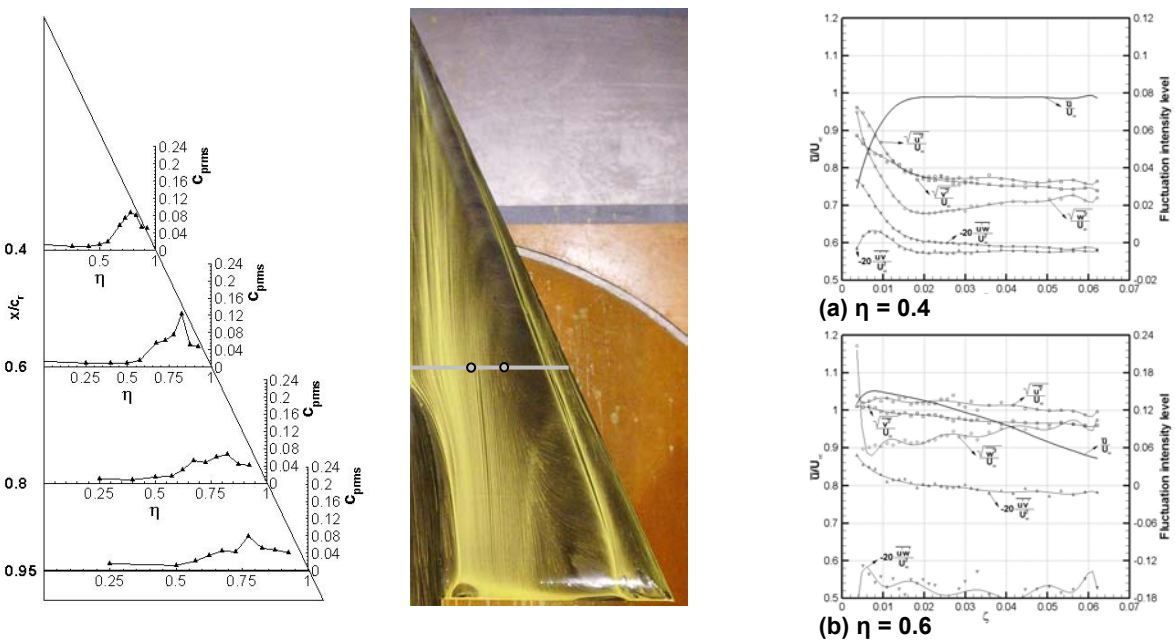

Figure 21-29: Surface Pressure Fluctuation Intensity (left), Surface Flow (middle) and Boundary Layer Profiles (right) for Sharp Leading Edge in Section $x/c_r = 0.6$ at α = 13°, $R_{mac} = 1 \times 10^6$ and M = 0.07.

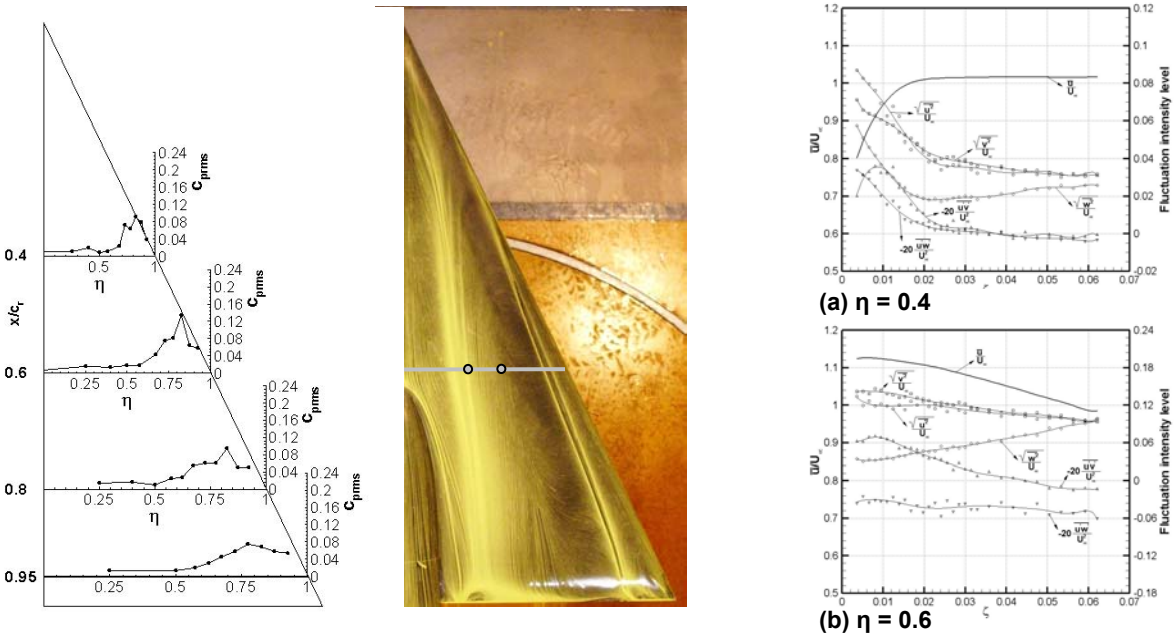

Figure 21-30: Surface Pressure Fluctuation Intensity (left), Surface Flow (middle) and Boundary Layer Profiles (right) for Rounded Leading Edge in Section x/c_r = 0.6 at α = 13°, R_{mac} = 1 x 10^6 and M = 0.07.

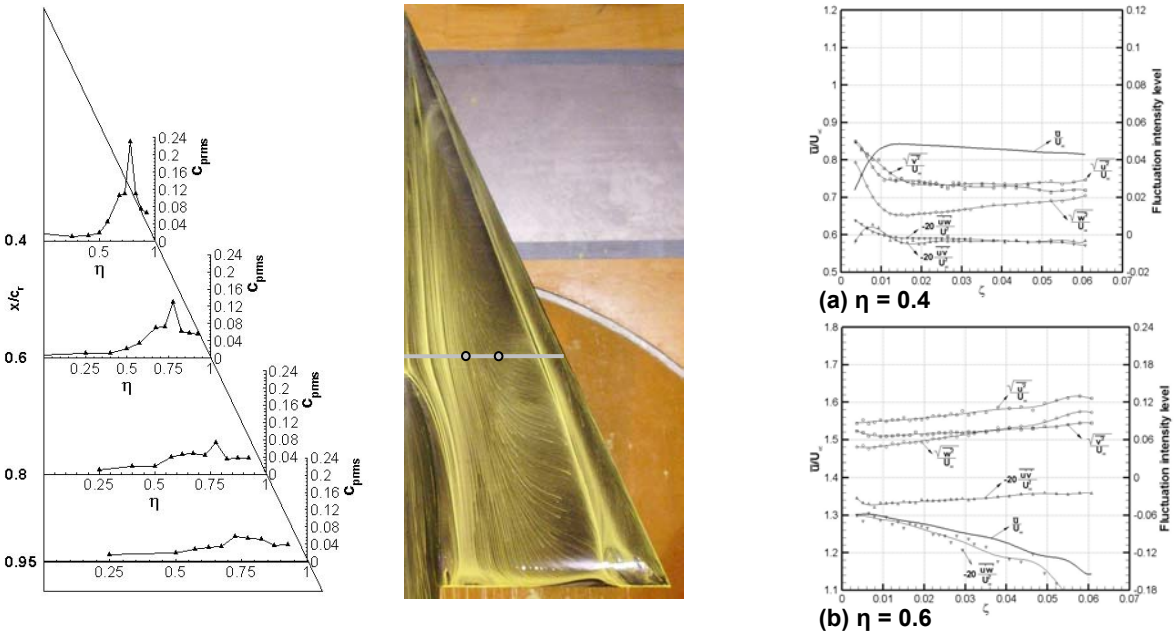

Figure 21-31: Surface Pressure Fluctuation Intensity (left), Surface Flow (middle) and Boundary Layer Profiles (right) for Sharp Leading Edge in Section x/c_r = 0.6 at α = 18°, R_{mac} = 1 x 10^6 and M = 0.07.

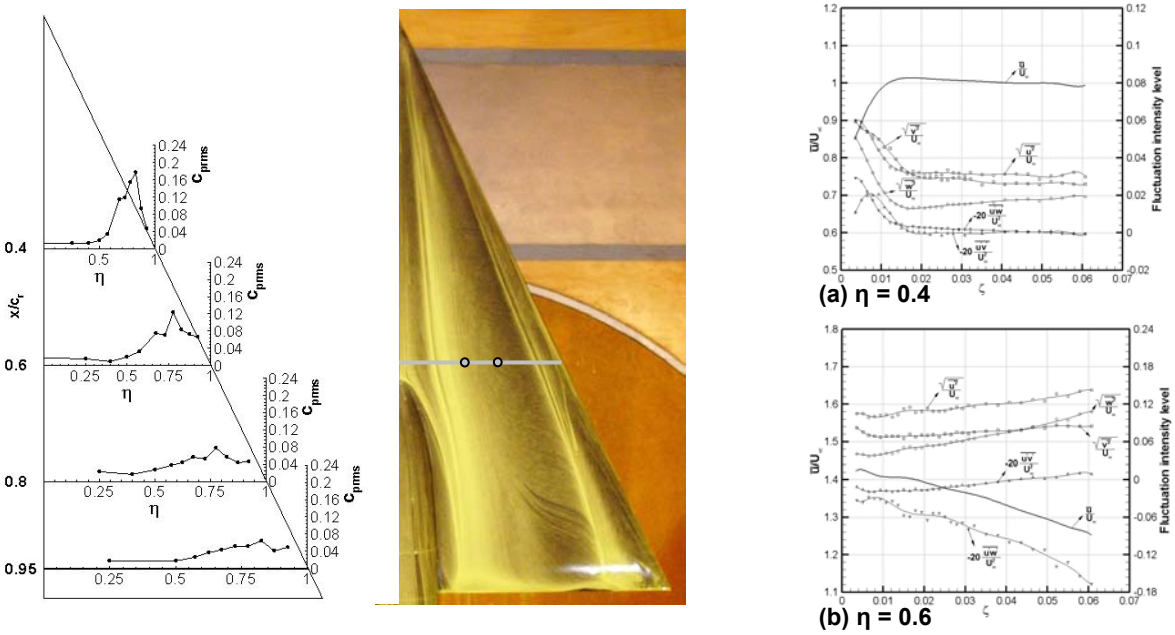

Figure 21-32: Surface Pressure Fluctuation Intensity (left), Surface Flow (middle) and Boundary Layer Profiles (right) for Rounded Leading Edge in Section x/c_r = 0.6 at α = 18°, R_{mac} = 1 x 10^6 and M = 0.07.

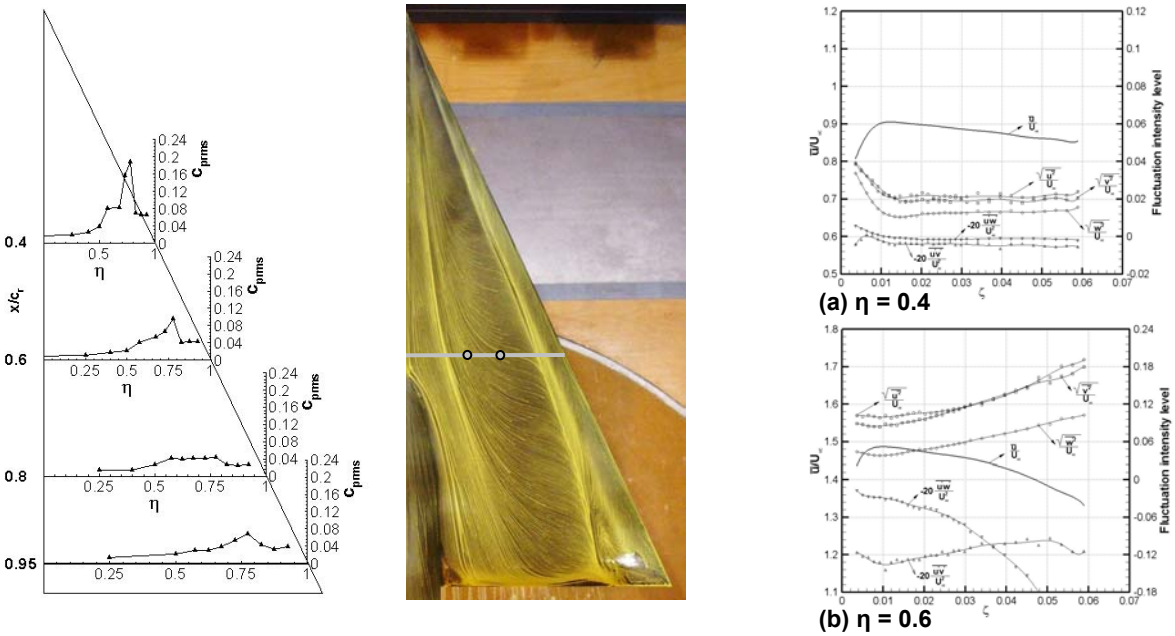

Figure 21-33: Surface Pressure Fluctuation Intensity (left), Surface Flow (middle) and Boundary Layer Profiles (right) for Sharp Leading Edge in Section x/c_r = 0.6 at α = 23°, R_{mac} = 1 x 10^6 and M = 0.07.

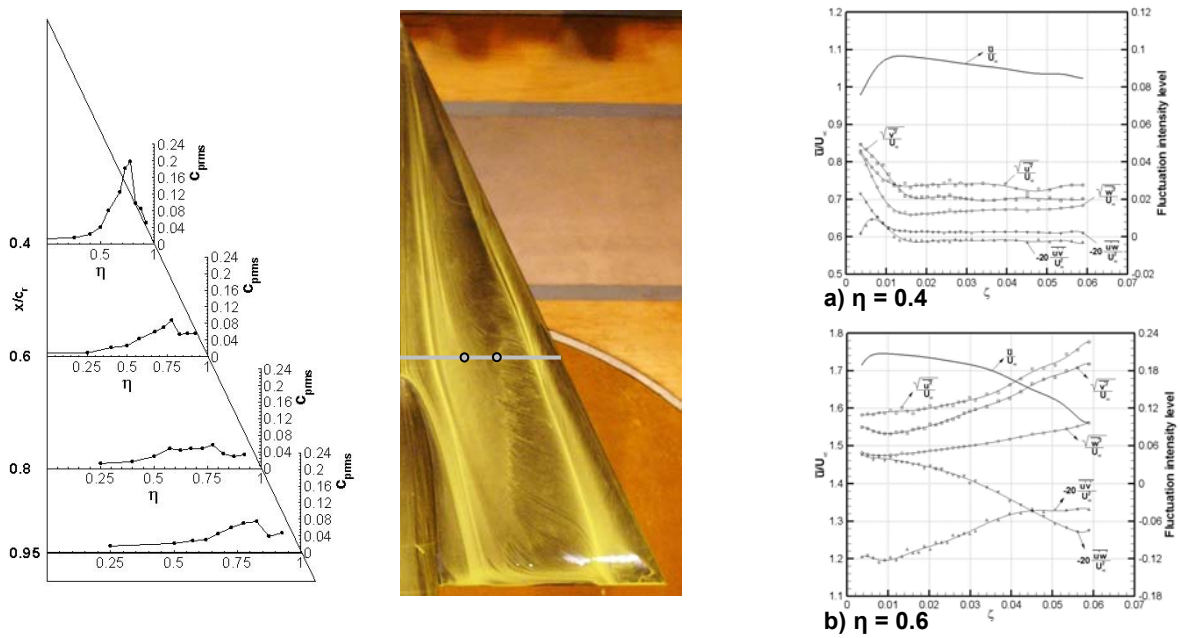

Figure 21-34: Surface Pressure Fluctuation Intensity (left), Surface Flow (middle) and Boundary Layer Profiles (right) for Rounded Leading Edge in Section x/c_r = 0.6 at α = 23°, R_{mac} = 1 x 10^6 and M = 0.07.

21.5 CONCLUSIONS AND OUTLOOK

Extensive experimental investigations on a delta wing model with a leading-edge sweep of 65 deg have been performed in the low-speed wind tunnel facilities A and B of the Institute of Aerodynamics at the Technische Universität München. The results contribute to the research work conducted within the International Vortex Flow Experiment 2 (VFE-2). The experiments performed contain different measurement techniques, like flow visualization using laser light sheet technique and oil flow technique, steady and unsteady surface pressure measurements, flow field velocity measurements using Stereo Particle Image Velocimetry and hot-wire anemometry, and boundary layer measurements based on hot-wire anemometry.

For the delta wing vortical flow structure some new and significant results are obtained, especially, when considering a rounded leading-edge:

- For medium angles of attack, a new flow phenomenon was found for delta wings with straight leading-edge depending strongly on Reynolds number. In addition to the classical primary vortex an inboard vortex occur close to the wing surface. This phenomenon appears stronger for the rounded than for the sharp leading-edge. While the primary vortex develops from the trailing-edge towards the apex with increasing angle of attack and therewith starts here from a turbulent separation, a laminar separation occurs at the wing surface in the region of the apex close to the symmetry plane. The flow is attached around the leading-edge, but the pressure increases towards the symmetry plane of the wing causing laminar separation in the inboard area. Downstream, the three-dimensional separation bubble transforms to a spatially small and weak vortex, which is situated close to the wing surface along the entire chord length.

- At high angle of attack, vortex breakdown dominates the wing flow associated with a characteristic annular region of local turbulence maxima surrounding the strongly expanded core of the burst primary vortex. Further, a narrow-band concentration of turbulent kinetic energy takes place. During the upstream movement of the breakdown location the turbulent flow field affects more and more the wing surface flow, thereby increasing the surface pressure fluctuations which also show coherent structures and significant concentrations in a certain frequency domain.
- Measurements of the boundary layer allow the quantification of the time averaged velocities as well as of the turbulent normal- and shear stresses close to the wing surface. For the Reynolds numbers investigated here and medium angles of attack, a turbulent boundary layer starts to develop at approximately 20% to 30% of the root chord for the attached flow in the inner part of the wing. Under the primary vortex the boundary layer becomes thinner by a factor of 2 to 5 due to the strong accelerated flow.

The comprehensive data base will be further evaluated and analyzed to improve the knowledge on the turbulent and unsteady flow quantities associated with the different stages of leading-edge vortex development.

21.6 ACKNOWLEDGEMENTS

The support of this investigation by the German Research Association (DFG) is gratefully acknowledged. The authors would also like to thank the VFE-2 partners for the fruitful and excellent co-operation.

21.7 REFERENCES

[21-1] Breitsamter, C.: *Unsteady Flow Phenomena Associated with Leading-Edge Vortices*, Progress in Aerospace Sciences, Vol. 44, No. 1, January 2008, pp. 48-65.

[21-2] Breitsamter, C.: *Turbulente Strömungsstrukturen an Flugzeugkonfigurationen mit Vorderkantenwirbeln*, Dissertation, Technische Universität München, Herbert Utz Verlag, ISBN 3-89675-201-4, 1997.

[21-3] Breitsamter, C. and Laschka, B.: *Turbulent Flow Structure Associated with Vortex-Induced Fin Buffeting*, Journal of Aircraft, Vol. 31, No. 4, 1994, pp. 773-781.

[21-4] Breitsamter, C.: *Experimentelle Untersuchung der instationären Feldgrößen und Oberflächendrücke bei wirbeldominierter abgelöster Strömung an einem Deltaflügel*, Jahrbuch der DGLR, Vol. I, DGLR-JT95-062, 1995, pp. 163-175.

[21-5] Breitsamter, C. and Laschka, B.: *Fin Buffet Pressure Evaluation Based on Measured Flowfield Velocities*, Journal of Aircraft, Vol. 35, No. 5, 1998, pp. 806-815.

[21-6] Breitsamter, C.: *Strake Effects on the Turbulent Fin Flowfield of a High-Performance Fighter Aircraft*, NNFM, Vol. 72, Vieweg Verlag, 1999, pp. 69-76.

[21-7] Chu, J. and Luckring, J.M.: *Experimental Surface Pressure Data Obtained on 65° Delta Wing Across Reynolds Number and Mach Number Ranges*, NASA-TM-4645, 1996.

[21-8] Crippa, S. and Rizzi, A.: *Numerical Investigation on Reynolds Number Effects on a Blunt Leading-Edge Delta Wing*, AIAA Paper 2006-3001, June 2006.

[21-9] Crippa, S. and Rizzi, A.: *Initial Steady/Unsteady CFD Analysis of Vortex Flow Over the VFE-2 Delta Wing*, ICAS-2006-P2.18, 25th Congress of the International Council of the Aeronautical Sciences, Hamburg, Germany, 3-8 September 2006.

[21-10] Elsenaar, A., Hjelmberg, L., Bütefisch, K. and Bannink, W.J.: *The International Vortex Flow Experiment*, AGARD-CP-437, Validation of Computational Fluid Dynamics, Lisbon, Portugal, May 2-5, 1988, pp. 9-1-15-23.

[21-11] Furman, A. and Breitsamter, C.: *Delta Wing Steady Pressure Investigations for Sharp and Rounded Leading Edges*, New Results in Numerical and Experimental Fluid Mechanics V, NNFM Vol. 92, 2006, pp. 77-84.

[21-12] Furman, A. and Breitsamter, C.: *Investigations of Flow Phenomena on Generic Delta Wing*, ICAS-2006-3.1.2, 25th Congress of the Int. Council of the Aeronautical Sci., Hamburg, Germany, 3-8 September 2006.

[21-13] Furman, A. and Breitsamter, C.: *Stereo-PIV and Hot-Wire Investigations on Delta Wing with Sharp and Rounded Leading Edge*, CEAS-2007-430, 1st CEAS European Air and Space Conference, Berlin, Germany, 10-13 September 2007, pp. 1749-1761.

[21-14] Furman, A. and Breitsamter, C.: *Turbulent and Unsteady Flow Characteristics of Delta Wing Vortex Systems*, AIAA Paper 2008-381-736, January 2008.

[21-15] Gursul, I.: *Unsteady Flow Phenomena Over Delta Wings at High Angle of Attack*, AIAA Journal, Vol. 32, No. 2, 1994, pp. 225-231.

[21-16] Gursul, I. and Xie, W.: *Buffeting Flows Over Delta Wings*, AIAA Journal, Vol. 37, No. 1, 1999, pp. 58-65.

[21-17] Hoeijmakers, H.W.M.: *Modelling and Numerical Simulation of Vortex Flow in Aerodynamics*, AGARD-CP-494, 1991, pp. 1-1-1-46.

[21-18] Hummel, D.: *On the Vortex Formation Over a Slender Wing at Large Angles of Incidence*, AGARD-CP-247, High Angle of Attack Aerodynamics, Sandefjord, Norway, October 4-6, 1978, pp. 15-1-15-17.

[21-19] Hummel, D.: *Documentation of Separated Flows for Computational Fluid Dynamics Validation*, AGARD-CP-437, Validation of Computational Fluid Dynamics, Vol. 2, Lisbon, Portugal, May 2-5, 1988, pp. 18-1-18-24.

[21-20] Hummel, D. and Redeker, G.: *A New Vortex Flow Experiment for Computer Code Validation*, Vortex Flow and High Angles of Attack, Loen, Norway, May 7-11, 2001.

[21-21] Hummel, D.: *Effects of Boundary Layer Formation on the Vortical Flow Above Slender Delta Wing*, RTO-MP-AVT-111, Paper 30, Symposium on Enhancement of NATO Military Flight Vehicle Performance by Management of Interacting Boundary Layer Transition and Separation, Prague, Czech Republic, 4-7 October 2004.

[21-22] Hummel, D.: *The Second International Vortex Flow Experiment (VFE-2): Objectives and Present Status*, AIAA Paper 2007-4446, June 2007.

[21-23] Luckring, J.M.: *Reynolds Number, Compressibility, and Leading-Edge Bluntness Effects on Delta-Wing Aerodynamics*, ICAS-2004-4.1.4, 24th Congress of the International Council of the Aeronautical Sciences, Yokohama, Japan, 29 August – 3 September 2004.

[21-24] Mitchell, A.M., Molton, P., Barberis, D. and Delery, J.: *Characterization of Vortex Breakdown by Flow Field and Surface Measurements*, AIAA Paper 2000-0788, 2000.

[21-25] Müller, J. and Hummel, D.: *Time-Accurate CFD Analysis of the Unsteady Flow on a Fixed Delta Wing*, AIAA Paper 2000-0138, 2000.

[21-26] Rai, P., Finley, D.B. and Ghaffari, F.: *An Assessment of CFD Effectiveness for Vortex-Flow Simulation to Meet Preliminary Design Needs*, Vortex Flow and High Angles of Attack, Loen, Norway, May 7-11, 2001.

[21-27] Schiavietta, L.A., Badcock, K.J. and Cummings, R.M.: *Comparison of DES and URANS for Unsteady Vortical Flows Over Delta Wings*, AIAA Paper 2007-1085, January 2007.

Copyright © 2008 by C. Breitsamter and A. Furman. Published by RTO with permission.